

Key Points:

- A time-domain Boussinesq model reproduced wave interference observed at Ocean Beach, CA
- The model reveals small-scale persistent fingering structures in the wave height distribution tied with nearshore flow structures
- Alongshore-varying wave breakers caused by wave interference are the source of vorticity generation, inducing energetic vortex eddies nearshore

Correspondence to:

F. Shi,
fyshi@udel.edu

Citation:

Zhang, Y., Shi, F., Kirby, J. T., & Feng, X. (2022). Phase-resolved modeling of wave interference and its effects on nearshore circulation in a large ebb shoal-beach system. *Journal of Geophysical Research: Oceans*, 127, e2022JC018623. <https://doi.org/10.1029/2022JC018623>

Received 10 MAR 2022

Accepted 30 SEP 2022

Author Contributions:

Conceptualization: Fengyan Shi
Investigation: Yu Zhang, Fengyan Shi, James T. Kirby
Methodology: Yu Zhang, Fengyan Shi
Supervision: Fengyan Shi
Validation: Yu Zhang, Xi Feng
Writing – original draft: Yu Zhang
Writing – review & editing: Fengyan Shi, James T. Kirby, Xi Feng

Phase-Resolved Modeling of Wave Interference and Its Effects on Nearshore Circulation in a Large Ebb Shoal-Beach System

Yu Zhang^{1,2}, Fengyan Shi² , James T. Kirby² , and Xi Feng¹ 

¹College of Harbor, Coastal and Offshore Engineering, Hohai University, Nanjing, China, ²Center for Applied Coastal Research, Department of Civil and Environmental Engineering, University of Delaware, Newark, DE, USA

Abstract A time-domain Boussinesq model was applied to modeling wave interference and its effects on nearshore circulation in San Francisco Bar and the adjacent Ocean Beach, CA. The model predicted the wave interference phenomena caused by the ebb shoal, with interference scales consistent with the radar observation and are persistent with nodal lines unchanged with time. Nearshore circulation predicted by the model shows small-scale flow structures tied with the wave modulation patterns. However, the small-scale modulation in the wave field seems not to generate alongshore variation in wave setup at similar scales. Therefore, in a large-scale view, the alongshore currents predicted by the Boussinesq model still keep the general features shown in a wave-averaged model, such as the flow divergence caused by the pressure gradient force associated with the alongshore variation of wave setup. The further analysis based on idealized short crest waves on a plane beach suggests that the alongshore pressure gradient is mainly balanced by the gradient of radiation stresses in the antinodal region, while by the flow advection in the nodal region. The rip current behavior is forced locally near breakers, rather than by gradients in wave setup close to shore. The time-domain Boussinesq model predicted the spatial variability of wave-induced processes. The alongshore-varying wave breakers caused by wave interference are the source of the vorticity generation, inducing energetic vortex eddies nearshore.

Plain Language Summary Ocean wave interference, caused by the oblique interaction or superposition of two or more trains of plane waves, is a common phenomenon caused by surface wave interaction with seabed topography, nearshore structures, or coastal currents. Conventional spectral wave models cannot predict interference patterns as they do not preserve phase information for the individual wave components. The objective of the present study is to use a time-resolved model to examine previously observed wave interference occurring landward of the ebb-tidal delta offshore of the Golden gate, San Francisco, CA. The model shows interesting small-scale features caused by wave interference, with spatial scales consistent with the radar measurements. The model results reveal that the small-scale fingering structures in the wave height distribution result in a significant alongshore variation in nearshore circulation and energetic vortex eddies in the surf zone, but do not induce a small-scale modulation in wave setup at the shoreface. To explain the phenomena, we carried out a momentum balance analysis for an idealized case of two intersecting waves propagating onto a plane beach, and show that the alongshore variability in forcing needed to balance variations in set-up is largely absent landward of where breaking becomes saturated in the alongshore direction.

1. Introduction

Coherent wave interference commonly occurs in the coastal ocean due to surface wave interaction with the inner-shelf topography, coastal structures, or coastal currents (Smit & Janssen, 2013). It is more significant for narrow-band waves, i.g., swells, which exhibit persistent wave height variability in the laboratory (Chawla et al., 1998; Vincent & Briggs, 1989) and field (Smit et al., 2016). Breaking waves under such coherent interference influences can generate nearshore circulation cells, which are more stationary (Dalrymple, 1975; Dalrymple et al., 2011) in contrast to transient circulation cells induced by non-coherent short-crested waves (Johnson, 2004; Spydell & Feddersen, 2009).

Modeling of coherent wave interference and associated wave-induced processes is challenging, especially at field scale. Traditional field-scale wave prediction models, such as Simulating WAves Nearshore (SWAN) (Booij et al., 1999) or WaveWatch (Tolman, 1991), are stochastic models based on the radiative transfer equation, which requires the assumptions for a slowly varying medium and statistically independent wave components (Komen et al., 1996). Such assumptions make the model unable to resolve inhomogeneous wave patterns caused by

coherent wave interference. These limitations have been partially alleviated by the recent work of Smit and Janssen (2013), who introduced the second-order statistics into a stochastic wave model, allowing the modeling of statistical wave interference caused by wave refraction and diffraction in coastal seas. The model was validated against in situ data measured during the Nearshore Canyon experiment in the Scripps and La Jolla Canyon (Smit et al., 2015), which showed that the model based on the quasi-coherent statistical theory is able to predict statistical interference and associated inhomogeneities in the wave field. More recently, Akrish et al. (2020) have extended the quasi-coherent model to include the effect of wave-current interaction.

A more direct way to model wave interference is to use phase-resolving wave models, such as Boussinesq models (e.g., Shi et al., 2012) or non-hydrostatic models (e.g., Ma et al., 2012). Because wave phase information is explicitly retained, the wave interference caused by wave coherence can be directly modeled. Another advantage in using such a phase-resolving wave model is that the model predicts not only wave interference patterns but also wave-wave interaction and breaking-induced nearshore circulation. However, due to the high computational cost of a phase-resolving model, large-domain field applications of such models have rarely been carried out.

Among the available classes of phase-resolving wave model, Boussinesq-type wave models are less time-consuming than non-hydrostatic wave models using a Pressure Poisson solver (e.g., NHWAVE or SWASH Ma et al., 2012; Zijlema et al., 2011). The parallel computing and the adaptive mesh refinement techniques make the model readily feasible to be used for simulations of surface wind waves over domains with dimensions of tens of kilometers (e.g., Chakrabarti et al., 2017].

The objective of this study is to investigate wave interference patterns arising in propagation of nearly unidirectional waves over bathymetry control and small-scale variability in shoreline circulation patterns using a phase resolving model approach. The study site is the San Francisco Bar and the adjacent Ocean Beach as shown in Figure 1.

Figure 1 shows the San Francisco Bar and the adjacent Ocean Beach. Smit et al. (2016) reported X-band radar observations which showed strong wave interference patterns in the nearshore region (see Figure 3 in Smit et al., 2016). Their analysis using the coupled-mode spectrum revealed that, during energetic swell events, the nearshore wave field is comprised of two coherent wave trains originating from the same offshore wave source. Due to wave refraction over the San Francisco Bar, the offshore waves are directionally separated into two swell systems behind the bar, resulting in a coherent interference pattern landward of the bar region. Figure 1b illustrates the wave interference pattern seen in Google Earth imagery taken on 14 March 2000. The wave height measured at the offshore Coastal Data Information Program (CDIP) buoy 029 (<http://cdip.ucsd.edu>), located at 37°56'45"N, 23°28'12"W, varied from 1.45–2.14 m on that day, with peak wave periods of 9.8–16.7 s. The averaged incident angle was 288°.

The influence of the San Francisco Bar on nearshore hydrodynamics and sediment transport has been investigated by many researchers. The San Francisco Bar is a large-scale horseshoe-shaped ebb-tidal delta as shown in Figure 1a. Earlier studies have shown the effect of wave focusing by the southern shoal, resulting in alongshore variations of wave energy and wave set-up along the adjacent Ocean Beach (Barnard et al., 2012; Eshleman et al., 2007; Hansen et al., 2014; Shi et al., 2011). The alongshore pressure gradient caused by wave set-up variation is the dominant force in the alongshore momentum balance, driving nearshore circulation and sediment transport on the beach (Hansen et al., 2013; Shi et al., 2011).

Numerical models used in previous studies of this region have been based on coupled wave and circulation models, such as the Nearshore Community Model (NearCoM, Chen et al., 2014; Shi et al., 2005) and Delft3D (Lesser et al., 2004). The wave component in both models mentioned above is the wave model SWAN (Booij et al., 1999). Wave interference and its effect on nearshore circulation could not be modeled due to the phase-averaging nature of the model theory. Our questions are (a) how does the wave interference affect the wavefield in the nearshore region of Ocean Beach; (b) how does the wave interference affect wave-induced circulation; (c) what is the difference in model prediction between a phase-averaging model and phase-resolving model.

To address these questions, we carried out a numerical study using the time-domain Boussinesq wave model, FUNWAVE-TVD, in a large-scale domain (10's km) to cover the entire wave propagation and evolution process, including wave shoaling, refraction, interference, breaking, and wave-induced nearshore circulation. The

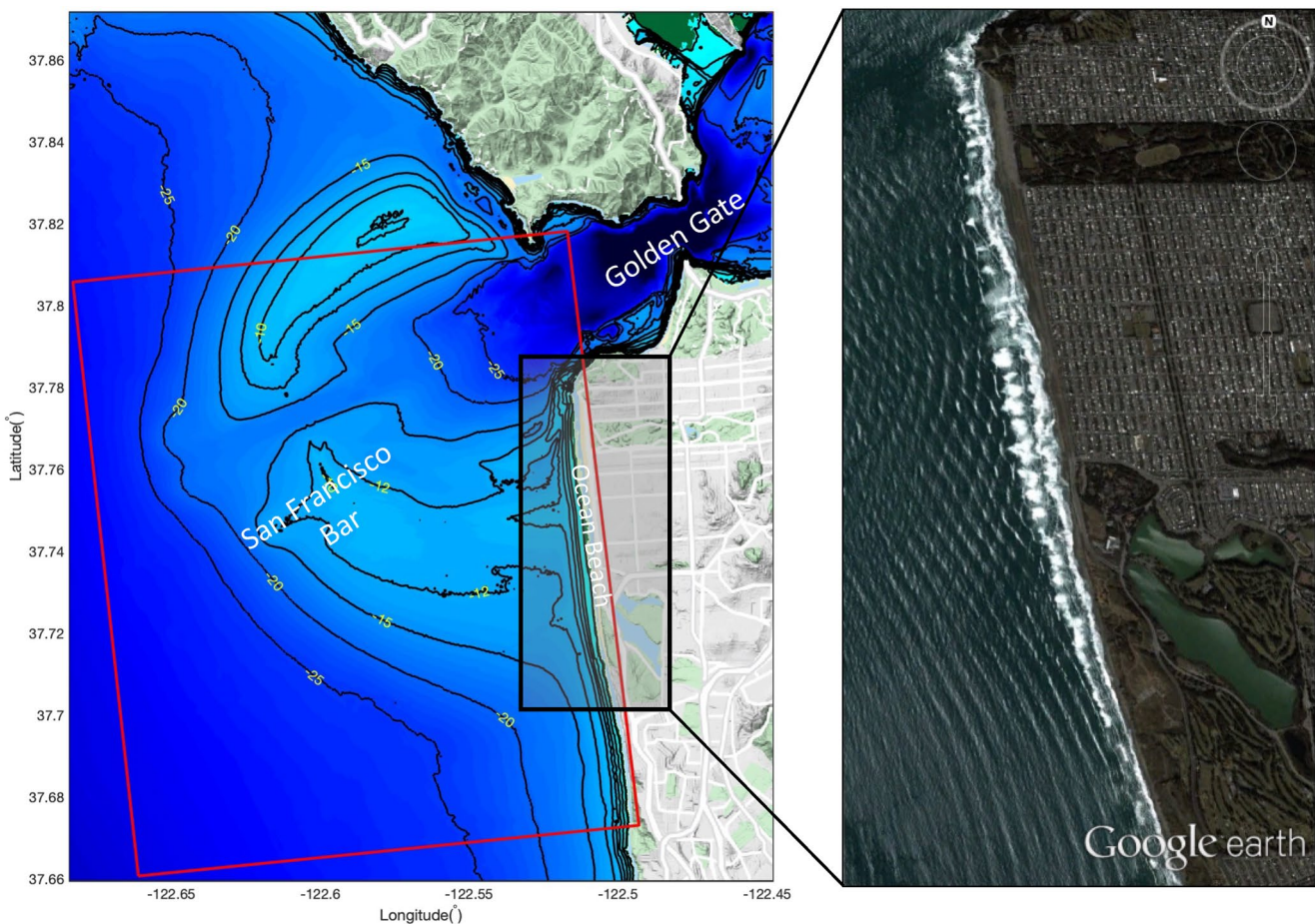


Figure 1. (left) the ebb tidal delta (San Francisco Bar) and Ocean Beach. The computational domain is denoted by the red block. Solid black lines are depth contours. (right) interference patterns of swells at Ocean Beach observed in the Google Earth imagery taken on 14 March 2000 (map ©2021 Google, ©TerraMetrics).

numerical results were compared with results from the coupled wave and circulation model, NearCoM, which cannot predict wave interference and its nearshore effects.

In the rest of the paper, Section 2 briefly reviews the study site and hydrodynamic conditions, emphasizing the wave interference phenomenon caused by the southern shoal. In Section 3, the numerical model and model setup are described. The basic characteristics of wave interference are presented using a monochromatic wave simulation and wave ray racing analysis in Section 4. Section 5 provides results of the wave field predicted by the Boussinesq model with comparisons with the measured data and model results from the phase-averaged model, SWAN. In Section 6, wave-averaged processes are discussed according to the comparisons between the Boussinesq model and the phase-averaged circulation model. Findings are summarized in Section 7.

2. Wave Interference Caused by San Francisco Bar

San Francisco Bar is a large-scale ebb-tidal shoal offshore of the Golden Gate of the San Francisco Bay as shown in Figure 1. The minimum depths are about 9.5 and 10.5 m on the northern and southern lobes, respectively. Shoreward of the south lobe is Ocean Beach, a 7-km long sandy beach located along the western, ocean-facing boundary of the city of San Francisco. The wave climate of Ocean Beach is characterized by large-scale wave height variability along the beach due to wave refraction over the shoal (Hansen et al., 2014; Shi et al., 2011). Nearshore circulation at this larger scale is governed by the alongshore pressure gradient generated by the variation in wave setup. It is also affected by the tide-induced alongshore pressure gradient due to the presence of the Golden Gate inlet (Hansen et al., 2013). Because Ocean Beach is directly exposed to energetic ocean swells, strong wave interference patterns occur at Ocean Beach, as reported by Smit et al. (2016). The wave interference

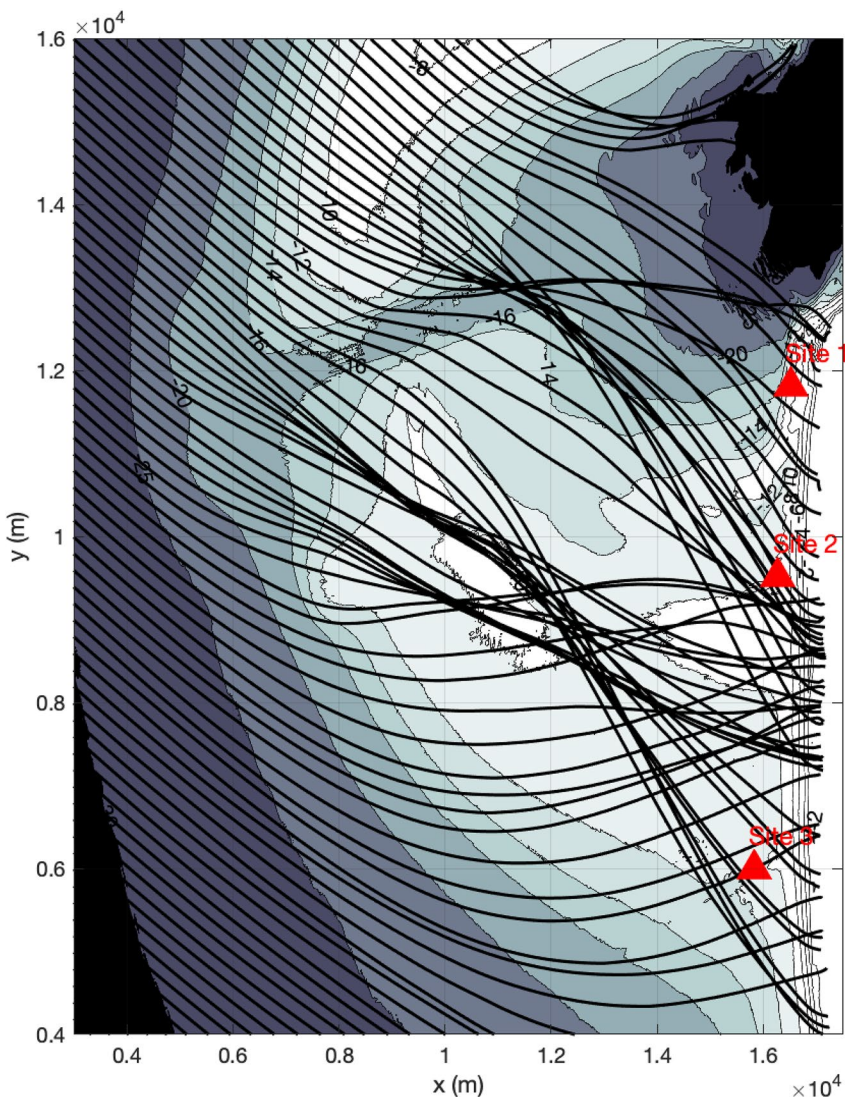


Figure 2. Wave ray tracing for offshore waves with an incident angle of $\theta = 300^\circ$ and a period of $T = 15$ s. Measurement locations, Site 1–Site 3 are denoted by red triangles. The wave ray crossing appears south of the nearshore measurement location, Site 2.

causes persistent wave height variability at the Ocean Beach, the effect of which on nearshore circulation is unknown.

Ocean swell with periods ranging from 11.4 to 26.6 s (O'Reilly et al., 2016) in this region is typically generated by large winter Pacific Ocean storms, which arrive from northwest to west. Lower-energy south swell events can occur during the summer, with a lower probability than the winter swell. According to the data measured during 1996–2021 at CDIP buoy 029 (<http://cdip.ucsd.edu>), located at $37^\circ 56' 45''\text{N}$, $23^\circ 28' 12''\text{W}$, more than 42% of wave events are swell waves, and about 70% of swell come from NWW with the averaging direction of 295° and an average period of 14.4 s.

To understand the wave interference caused by wave refraction over the shoal, we applied the wave tracing theory described in Mei et al. (2005) in the bathymetric domain as shown in Figure 2. The domain coordinates were rotated by 7° counter-clockwise to make the shoreline align with the y-direction in the local Cartesian coordinates (x, y). This rotation can facilitate the model setup described in the next section. Figure 2 shows the ray tracing results for offshore swell with a direction of 300° and a period of 15 s propagating over the San Francisco Bar and onto Ocean Beach. Each wave ray was obtained for given wave direction, period and initial position at the

domain boundaries. As shown in the figure, wave refraction over the shoal causes strong wave interference with significant wave-ray crossing at the nearshore region.

During the summer of 2005 and the winter of 2006, two field experiments were performed to examine spatial differences in wave and current patterns offshore of Ocean Beach (Barnard et al., 2007, Shi et al., 2011). Site 1–Site 3 are three measurement sites aligned approximately alongshore in water depths from 7 to 13 m. Detailed deployment locations and durations are referred to Shi et al. (2011).

3. Time-Domain Boussinesq Wave Model

FUNWAVE is a widely-accepted public domain Boussinesq-type wave model in the nearshore and tsunami research community. The original generation of the code was developed by Kennedy et al. (2000) and Chen et al. (2000), based on the fully nonlinear Boussinesq equations of Wei et al. (1995). Subsequent improvements in the formulation covering improvements in nonlinear mode-coupling (Kennedy et al., 2001) and treatment of the vertical component of vorticity (Chen, 2006; Chen et al., 2003) have been incorporated in the recent development of a Total Variation Diminishing (TVD) version, FUNWAVE-TVD, motivated by recent needs for modeling surfzone dynamics, tsunami waves, and coastal inundation processes in both global and coastal scales (Shi et al., 2012). The model has been parallelized using the message passing interface and optimized for use on large-scale, high-performance computing system (Lam et al., 2018). Extensions incorporating GPU-acceleration techniques (Yuan et al., 2020) will further increase the feasibility of the model's use for large-domain and long-time simulations. For irregular wave applications, the model is equipped with an internal wavemaker (see Wei et al., 1999) that can generate monochromatic or directional spectral waves based on bulk parameters or measured spectral data. Recently, the wavemaker has been revised to address the problem of spurious spatial correlations occurring in irregular waves, resulting from discretization of target spectra over a uniform grid of frequencies and alongshore wavenumbers (Salatin et al., 2021).

According to the model applicability related to the weakly dispersion assumption, $kh \leq 3$ (Kirby, 2016), we confine the computational domain nearshore up to the water depth of 35 m, covering the southern ebb-tidal shoal and Ocean Beach, as shown in Figure 1 (red block). The computational grid was constructed using the 10-m digital elevation model (DEM) (Fregoso et al., 2017), which combines bathymetry and topography data with the vertical datum of NAVD88. The mean tide level (MTL) was converted based on the datum at NOAA station 9414290 in San Francisco, CA. The grid has $8,712 \times 7,960$ grid points with grid sizes of 2×2 m, covering a region of 17.424 and 15.920 km in the x – and y – directions, respectively.

We applied the internal wavemaker, which can generate monochromatic and spectral waves for given directional spectra, such as Texel-Marsden-Arsloe (TMA spectra, Bouws et al., 1985), (JONSWAP spectra, Hasselmann et al., 1973), or measured spectral data. In the present study, the JONSWAP spectra was used to compare with the SWAN model. The wavemaker is located at a 35-m flat bottom (truncated near 35 m contour), 800 m away from the west boundary. A 500m-wide sponge layer was specified at the western boundary to absorb waves propagating seaward from the internal generation region. To apply the lateral periodic boundary condition, we modified the bathymetry and topography at the inlet region to make the grid cyclic in the south-north direction with a 4-km wide buffer region on the north side. Such a reconstruction of the grid does not affect modeled wave field nearshore of Ocean Beach because wave directions considered in this study are basically from NWW. A constant bottom drag coefficient of $C_d = 0.002$ in the quadratic friction formula was applied in all cases below.

4. Basic Characteristics of Wave Interference in a Monochromatic Wave Field

To demonstrate the basic characteristics of coherent wave interference caused by the tidal ebb shoal, we carried out a simulation of monochromatic waves with an incident angle of $\theta = 300^\circ$, a period of $T = 15$ s, and wave height of $H = 2$ m, which are typical bulk parameters for winter swells. Figure 3 provides a snapshot of wave surface elevation with wave ray tracing (thick lines) superimposed on the wave surface. The subplot (b) in Figure 3 provides a sketch of two intersecting plane waves, which is used for calculating the length of a standing wave cell later. Due to the modification for the periodic boundary condition mentioned above, the bathymetric contours in the figure are slightly different from that shown Figure 2 in the northern region. For this reason, the wave rays in the north of the domain are not shown. The figure shows that, before reaching the shoal, waves are regular plane

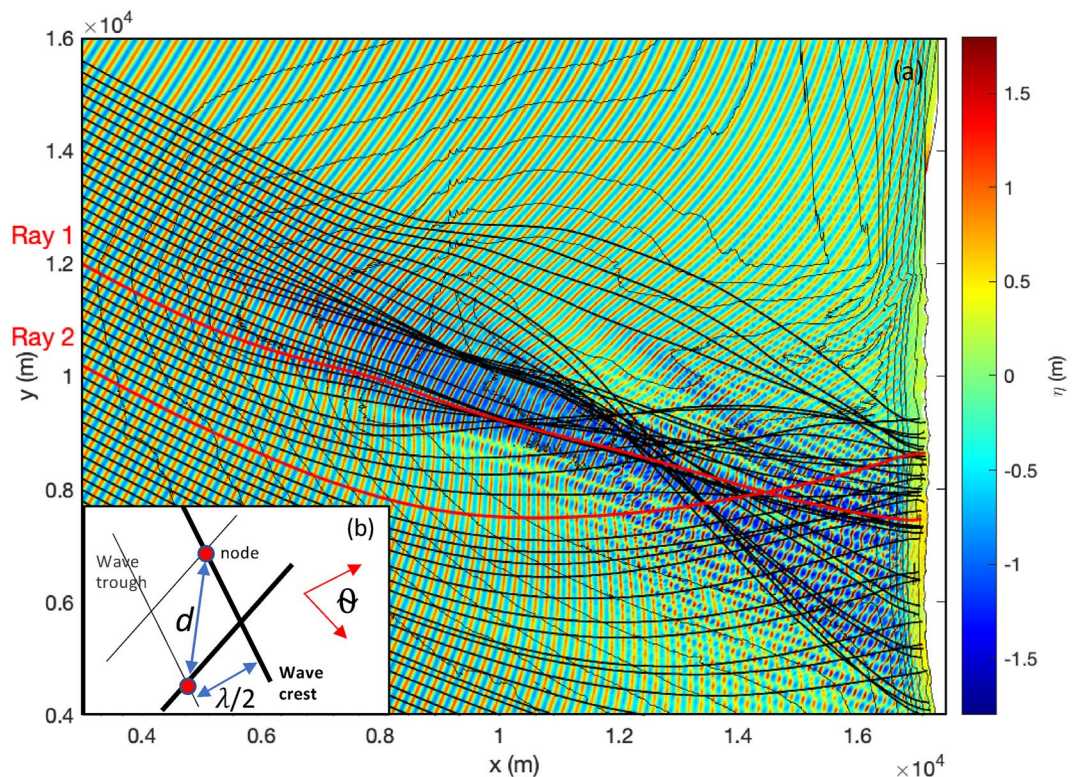


Figure 3. A snapshot of wave surface elevation (color) modeled for offshore monochromatic waves with an incident angle of $\theta = 300^\circ$, a period of $T = 15$ s. Thin solid lines are bathymetric contours, thick solid lines denote wave rays. The red solid lines represent two wave rays selected for 1D surface elevation plots in Figure 4. The nested subplot (b) shows a sketch used to calculate lengths (d) of standing wave cells. Thick black lines represent wave crests and thin black lines are for wave troughs. Red arrows represent wave propagation directions.

waves with approximately uniform wave height and direction. Wave shoaling effects are significant as waves climb over the shoal, as indicated by large peaks (sharp red color) and lower troughs (blue color) on the shoal. Wave refraction on the shoal causes convergence and divergence of wave rays, inducing larger wave heights in the focusing zone and lower wave heights in the shadow zones (both southern and northern sides of the focusing zone). Wave diffraction patterns are also shown in the shadow zone. Further nearshore, standing wave patterns caused by the wave interference appear in the wave-ray crossing region, which covers a similar area as the wave focusing zone. Waves break near the shoreline, inducing large wave setup as indicated by the warmer color in the surf zone, consistent with the wave setup patterns modeled by Shi et al. (2011).

Figure 4 shows the same snapshot as Figure 3, but are 1-D plots along two wave rays denoted by the red lines, Ray 1 and Ray 2, respectively, in Figure 3. Ray 1 traces waves across the top of the shoal, while Ray 2 is located south of Ray 1, passing the shadow zone. Along Ray 1, wave shoaling occurs as waves enter the shallow shoal (see bathymetric profile (b), $x < 10,000$ m). As waves continue propagating shoreward, a large variation in wave amplitude appears though the water depth shoreward is relatively flat (see b). The large variation in amplitude results from the standing wave patterns as revealed in Figure 3. In contrast to Ray 1, waves propagating along Ray 2 do not show shoaling-induced wave height increase because waves along Ray 2 are inside the shadow zone and the seabed slope is milder compared to the profile along Ray 1. However, large waves emerge nearshore ($x > 12,000$ m) as the wave ray bends northwards, entering the wave interference region.

The alongshore modulation scales represent the lengths of standing wave cells in the alongshore direction at a certain water depth, and can be calculated directly using the geometry of two intersecting plane waves, as shown in the subplot of Figure 3b. For a wave length λ and wave crossing angle θ derived from the wave rays at a certain water depth, the length of a standing wave cell can be evaluated by the distance of two adjacent nodes, $d = 0.5\lambda \sin(\theta/2)$. The length of a standing wave cell in the alongshore direction can be obtained by making a projection

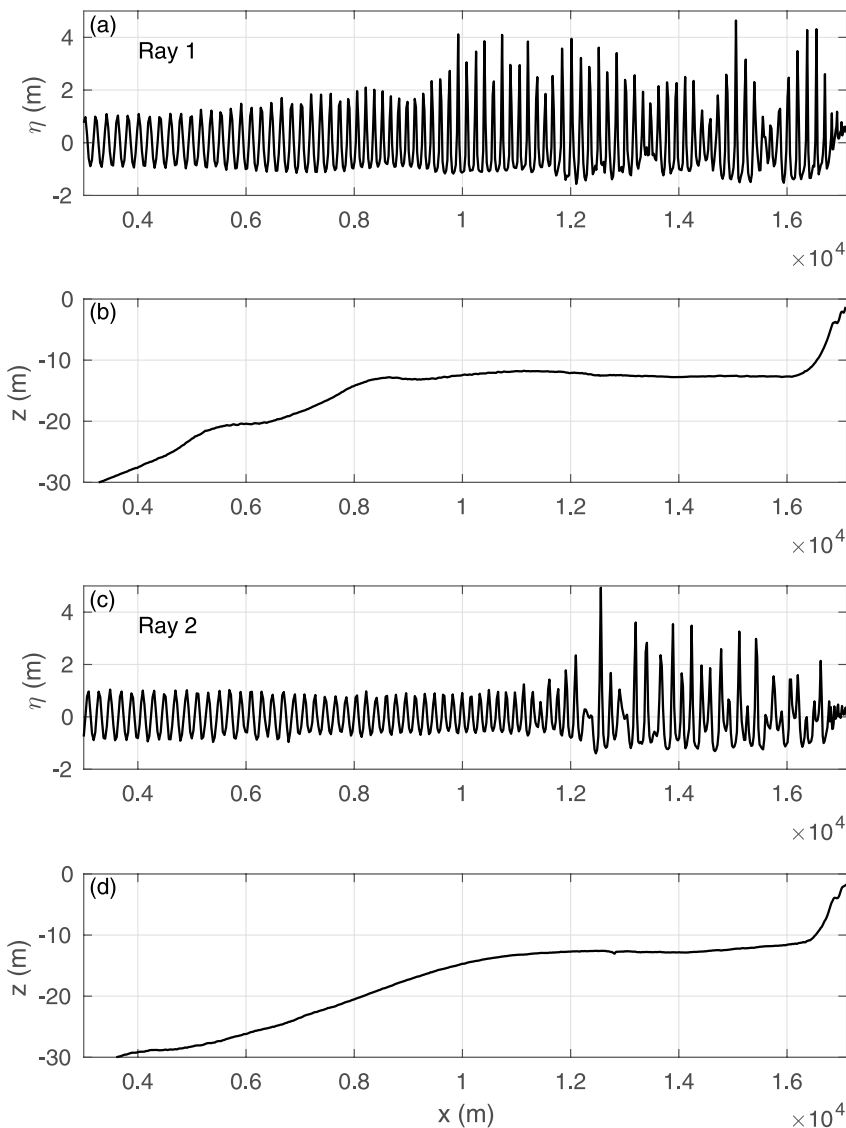


Figure 4. Snapshots of wave surface elevation (a, c) and bathymetric profiles (b, d) along the two wave rays selected in Figure 3.

of d onto the y -direction. Figure 5 shows lengths of standing wave cells in the alongshore direction at 10 m water depth offshore of Ocean Beach calculated based on wave tracing for waves of $T_p = 15$ s with different incident angles. It appears that the lengths of standing wave cells do not vary much with the incident wave angles, except for the incident angle of 165° , in which wave interference occurs at the northern part of Ocean Beach. The alongshore lengths are in $150 \sim 310$ m, which is generally consistent with the alongshore lengths of $100 \sim 300$ m observed in Smit et al. (2016). The lengths may change with the incident wave period and water depth.

5. Spectral Wave Field

5.1. Model Comparison to Radar Imagery

Coherent wave interference is difficult to observe using the traditional field observation techniques such as point measurements of wave and current signals. To verify the model capability of modeling the wave interference process, we carried out a simulation in the wave condition where the Radar data was observed by Smit et al. (2016). Figure 6a shows the radar map of the ocean surface observed on 10 January 2014, at 6:15 UT (Figure 3 in Smit et al., 2016). The wave conditions measured at the CDIP 029 buoy are the significant wave

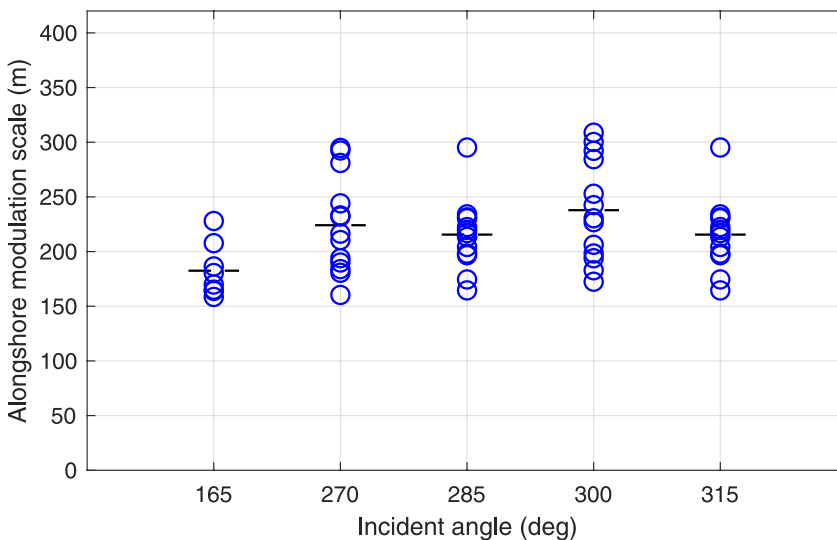


Figure 5. Lengths of standing wave cells in the alongshore direction at 10 m water depth calculated from wave tracing for offshore waves with different incident angles (Nautical Convention) and $T_p = 15$ s. Short black lines represent the values averaged over interference rays passing 10 m water depth contour.

height $H_s = 2.55$ m, peak wave period $T_p = 11.76$ s, and peak incident wave angle $\theta_p = 299^\circ$. An X-Band radar system was located at $37^\circ 43.69' N$, $122^\circ 30.34' W$. The Cartesian coordinate system has the origin at the radar site, and the axes x directed approximately alongshore (4° west of south) and y directed cross-shore (4° south of east). Coherent wave interference can be identified by the crossing wave crests shown in red color. A snapshot of wave surface elevation modeled by FUNWAVE was mapped in the same Cartesian system shown in Figure 6b. For a comparison, the radar coverage shown in (a) is highlighted by bright color in (b). The model result shows a similar wave interference pattern as the measurement with crossing wave crests offshore induced by two major wave components from north-west and south-east, respectively. In the nearshore region, the standing wave pattern become less significant probably because of wave breaking, which is generally consistent with the patterns in the radar imagery.

5.2. Simulations of Wave Conditions Observed During the Field Campaign

To investigate the wave interference and its effects on wave height distribution and wave-averaged nearshore processes, we selected two wave conditions that occurred during the observation periods in summer 2005 and winter 2006, respectively, both of which favor the generation of wave interference patterns in terms of wave incident angle. Case 1 simulates the wave condition appeared on 12 July 2005 with the significant wave height $H_s = 2.49$ m, the peak period, $T_p = 11.1$ s, and dominant wave angle $\theta_p = 290^\circ$ measured at the CDIP 029 buoy. Case 2 is a major storm event occurred on 4 January 2006 with $H_s = 5.1$ m, $T_p = 14.29$ s, and $\theta_p = 297^\circ$. The wave input conditions for the Boussinesq model are based on wave bulk parameters resulting from the large-domain model, NearCoM (Shi et al., 2011). The JONSWAP spectrum with $\gamma = 3.3$ and the directional spreading parameter $\sigma_\theta = 10^\circ$ was partitioned into 1125 wave components, which are randomly phased with zero-coherence (Salatin et al., 2021). The water depth is adjusted based on the tidal level recorded at the NOAA station 9414290.

Figure 7 shows a snapshot of surface elevation after a spin-up period of 1800 s. The figure shows wave shoaling at the ebb-shoal, focusing due to wave refraction, and remarkable standing wave features caused by wave interference, generally consistent with the regular wave case. The wave interference concentrates at the nearshore region south of Site 2, similar to the regular wave case due to the similar offshore incident angle.

Significant wave height was estimated using the zero-crossing method for the time period of 1800–3000 s in the simulation. As shown in Figure 8, large wave heights occur at the ebb-shoal region and the nearshore area behind the shoal due to wave focusing. In particular, wave height in the nearshore region exhibits fingering patterns arising from the oblique intersection of component waves, as in the monochromatic case, with magnitudes fluctuating in the alongshore direction.

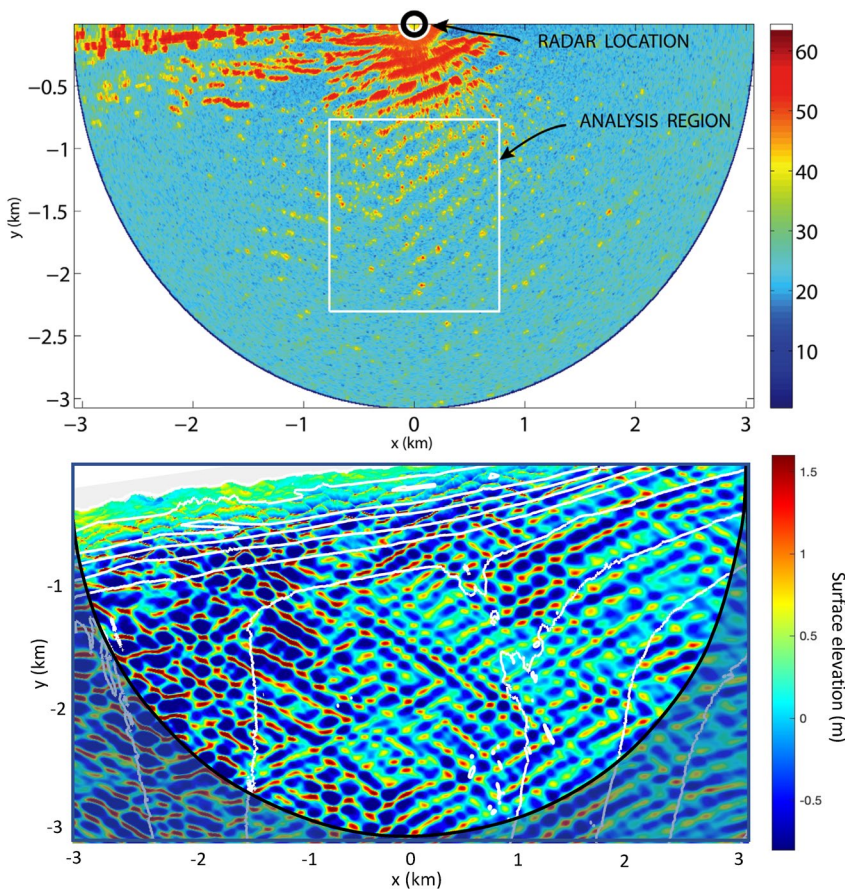


Figure 6. (a) Radar map of the ocean surface observed on 10 January 2014, at 6:15 UT by the X-Band radar system (Figure 3 in Smit et al., 2016). (b) A snapshot of wave surface elevation modeled by FUNWAVE with the wave condition occurred on 10 January 2014 with $H_s = 2.55$ m, $T_p = 11.76$ s, and $\theta_p = 299^\circ$ measured at the Coastal Data Information Program 029 buoy. The Cartesian coordinate system used here follows Smit et al. (2016) with x is directed 4° west of south and y is directed 4° south of east. Radar coverage is highlighted with bright color. White solid lines represent the bathymetric contours.

Figure 9a compares the modeled wave height with data along the wave measurement transect denoted by the white line in Figure 8. To examine the persistence of the wave height distribution, we calculated the wave height in the different averaging periods, 300 s, 600 s, and 1200 s, respectively, in the comparison. It is shown that, despite the different averaging periods used for wave height estimate, the recurring modulation patterns are similar with nodal locations approximately fixed, suggesting a pronounced persistent feature associated with wave interference. The magnitudes of fluctuation (from node to antinode) are around 1 m, with the maximum magnitude appearing at the center of the focusing region. Because the data at Site 1 is unavailable, the modeled wave heights are compared with the data at Site 2 and Site 3, respectively, with good agreement. The comparison also shows that the measurements are too sparse in space to capture the wave height fluctuation patterns.

Case 2 is a major storm condition with $H_s = 5.1$ m, $T_p = 14.29$ s, and $\theta_p = 297^\circ$ observed at CDIP 029 buoy. Because the wave incident angle is close to Case 1, the wave propagation and evolution patterns are similar to Case 1 and are thus not shown here. Figure 9b shows the same plot as (a) but for Case 2 (Note: the data is unavailable at Sites 1 and 2). Again, the fluctuation patterns in the alongshore wave height distribution are quite persistent, reflected by the fixed nodal locations obtained from different averaging periods. Compared to Case 1, which is for the normal wave condition, the alongshore variation of wave height in the storm condition is much larger, reaching 2 m. The effect of the larger wave height variation on nearshore circulation is expected to be stronger than that in the normal wave condition.

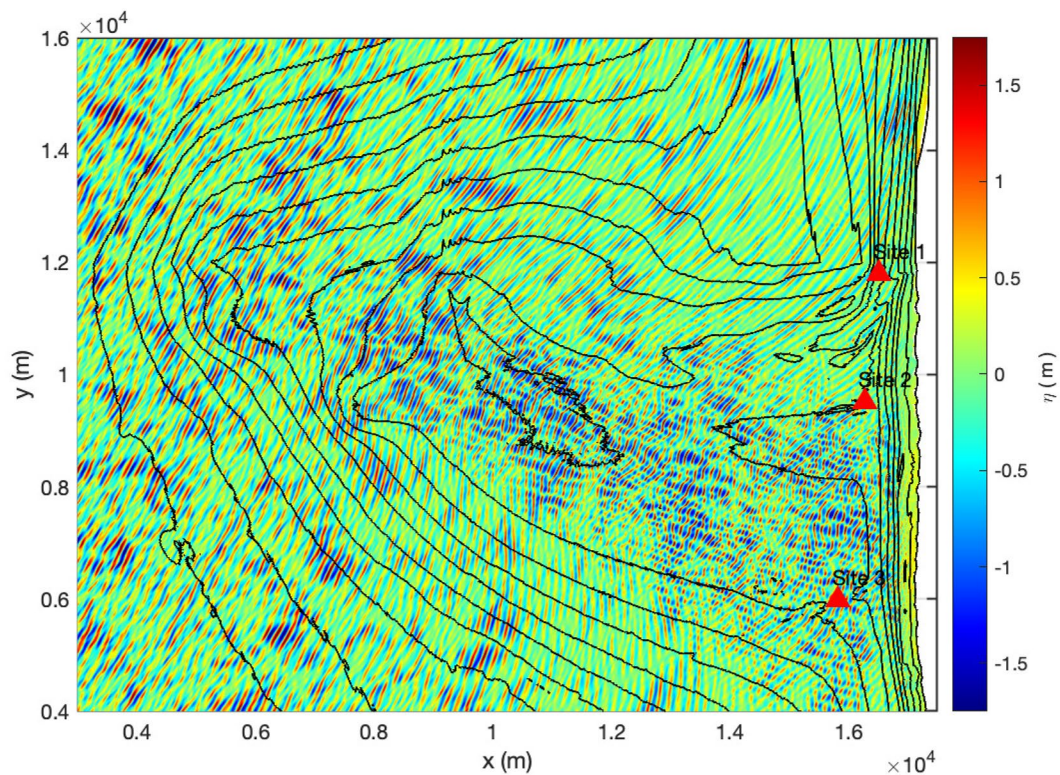


Figure 7. A snapshot of wave surface elevation (color) for Case 1 simulated by Boussinesq model. The wave condition occurred on 12 July 2005 with $H_s = 2.49$ m, $T_p = 11.1$ s, and $\theta_p = 290^\circ$ measured at the Coastal Data Information Program 029 buoy. Red triangles represent measurement locations, Site 1–3 (Hansen et al., 2013; Shi et al., 2011).

5.3. Comparison to the SWAN Model

It is interesting to compare the phase-resolving Boussinesq model and the conventional phase-averaged wave model that cannot model wave interference. The wave model in the previous studies of San Francisco Bar is the SWAN model, such as in NearCoM (Shi et al., 2011) and Delft-3D (Hansen et al., 2013). Here, we applied the NearCoM model with the same bathymetric data (modified periodic bathymetry) and the same wave conditions as FUNWAVE. To make the model comparable to FUNWAVE, we only considered the surface wave boundary condition, ignoring tidal current, wind, and other external forcing used in Shi et al. (2011). As a wave-averaged model, NearCoM does not resolve individual waves and thus a coarse grid can be used. A uniform rectangular grid was used with a grid resolution of 20 m, which is consistent with the grid resolution used in Shi et al. (2011).

Figure 10 shows the wave height distribution from the SWAN model. Wave focusing causes large wave heights mainly distributed on the shoal. Compared to the FUNWAVE results shown in Figure 8, the major difference between the two models can be found in the nearshore region, where FUNWAVE predicts the fingering patterns of the wave field, while SWAN provides a smooth distribution of wave height. A striking difference can be seen in the 1D plot of wave height comparisons along the measurement transect shown in Figure 9. The SWAN model does not predict the large magnitude fluctuations as in the FUNWAVE model. In addition, FUNWAVE predicts generally larger wave heights at the center of the focusing region than SWAN, probably due to different wave dissipation mechanisms in FUNWAVE, similar to the finding in Geiman et al. (2011) who also compared FUNWAVE and SWAN in the simulation of the Rip Current Experiment (RCEX, Brown et al., 2009; MacMahan et al., 2010).

6. Wave-Averaged Processes

The previous studies showed that the nearshore circulation at Ocean Beach exhibits remarkable alongshore variation. Although Ocean Beach has a nearly alongshore uniform bathymetry, the nearshore wave field is strongly alongshore varying because wave refraction over the ebb shoal causes wave focusing toward a narrow

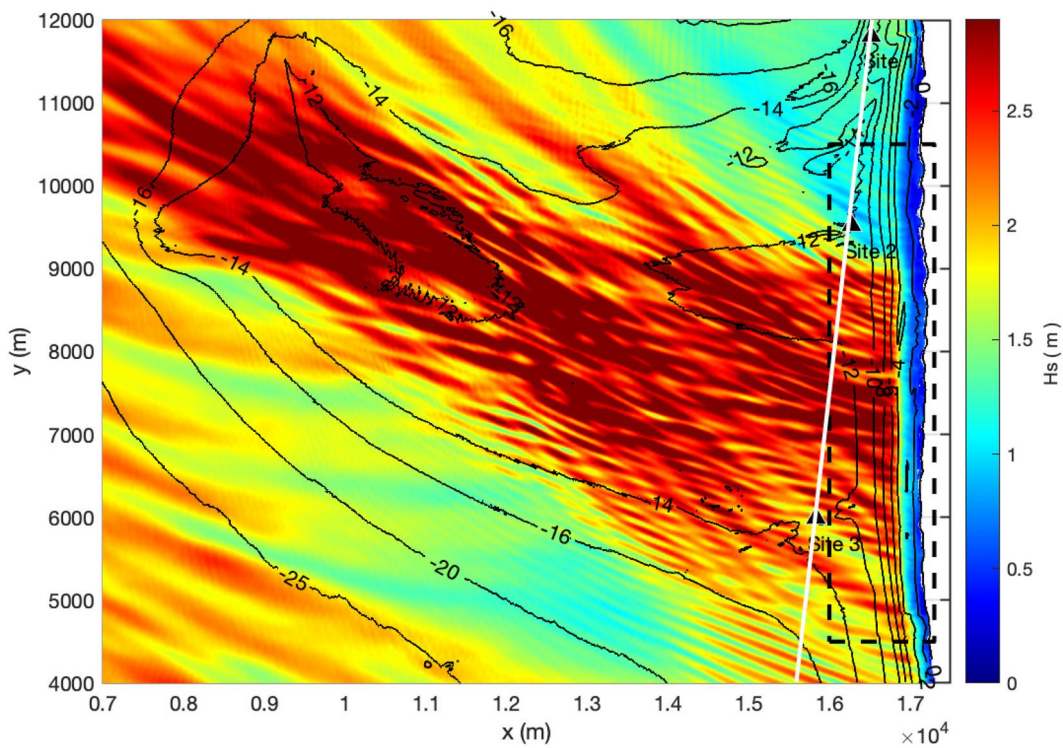


Figure 8. Distribution of the significant wave height estimated using zero-crossing in a time interval of 1200 s (1800 s–3000 s). Case 1: $H_s = 2.49$ m, $T_p = 11.1$ s, and $\theta_p = 290^\circ$ measured at the Coastal Data Information Program 029 buoy. Black triangles represent measurement locations, Sites 1–3. The rectangle bounded by black dashed lines is the region shown in Figure 11. The white line is the transect crossing the measurement locations, Site 1–Site 3.

region at Ocean Beach. Due to the spatial variation in wave breaker height, wave-induced setup appears to have a strong alongshore nonuniformity, resulting in a dramatic change in the pressure field (Hansen et al., 2014; Shi et al., 2011). The pressure gradient can be a dominant force driving nearshore circulation in the surf zone of Ocean Beach. For the time-domain Boussinesq model, wave-averaged quantities, such as wave setup, alongshore current and rip current velocities are usually obtained by wave averaging over a number of wave periods (Chen et al., 2003).

6.1. Wave-Averaged FUNWAVE Results

Figure 11 shows wave-averaged results from Case 1, including the significant wave height (a), wave setup (b), and nearshore circulation in the nearshore region denoted in the dashed line block in Figure 8. The wave-averaged quantities were calculated in a 1200 s-long time period starting from the simulation time of 1800 s–3000 s. As shown in (a), large wave heights are basically confined in the 5,000 m-long offshore region, $y = 5,000 \sim 9,000$ m, with the maximum value around the center of the region. Spatial modulation of wave height distribution caused by wave interference are in small-scale, in sizes of 200 ~ 300 m. Waves break in shallow water and induce wave setup in the surfzone (b). Due to the alongshore variation in offshore wave height, wave setup appears to be alongshore varying. It is interesting that the wave setup does not respond closely to the small-scale feature of the spatial modulation of offshore wave height and turns to be smoothly distributed alongshore. This phenomenon will be discussed in the following section. Figure 11c shows the wave-induced nearshore circulation with arrows representing current velocity vectors and color for alongshore component velocity (blue for southward). As waves come from northwest, alongshore currents are generally southward. However, the alongshore pressure gradient associated with alongshore nonuniform wave setup induces the northward forcing, causing flow reversal, or divergence, as shown in the north region (8,000 ~ 9,500 m). The pressure-gradient-driven process described here is consistent with the finding of Shi et al. (2011).

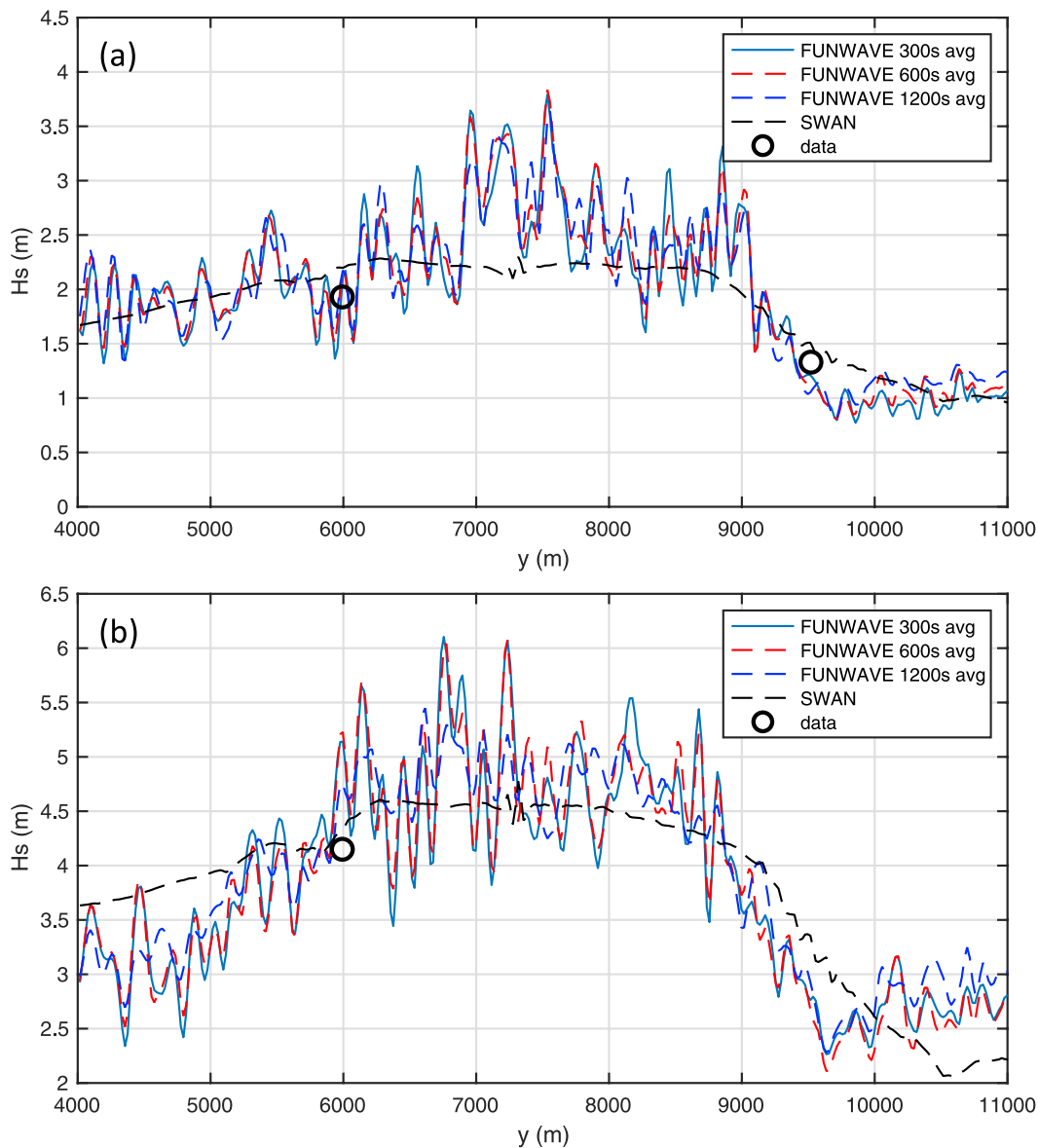


Figure 9. Alongshore wave height distributions estimated for averaging periods with durations of 300 s, 600 s, and 1,200 s along the wave measurement transect, Site 1–Site 3. (a) Case 1: $H_s = 2.49$ m, $T_p = 11.1$ s, and $\theta_p = 290^\circ$ measured at the Coastal Data Information Program (CDIP) 029 buoy. (b) Case 2: $H_s = 5.1$ m, $T_p = 14.29$ s, and $\theta_p = 297^\circ$ measured at the CDIP 029 buoy. The dashed line represents the result from the Simulating WAves Nearshore (SWAN) model, discussed in Section 5.2.

For the major storm condition simulated in Case 2, wave breaking-induced currents are more intensive compared to that in Case 1. In Figure 12, we illustrate wave-induced current field superimposed on the vertical vorticity field, which is representative of energy dissipation due to wave breaking and bottom friction according to the vorticity conservation equation (e.g., Chen et al., 1999). The storm waves break on the ebb shoal, generating apparent vortices on the shoal, which are absent in Case 1. Wave breaking induced currents on the shoal basically move in the same direction as the dominant wave direction, which can be explained by the major forcing term, $\mathbf{k}D_w$, where \mathbf{k} is the wavenumber vector and D_w is energy dissipation, in the vortex form of wave force formulation (Shi et al., 2007; Smith, 2006). In the nearshore region, the patterns of wave-induced current look similar to that in Case 1 but with a wider surfzone and larger current velocities caused by the overwhelming wave breaking nearshore.

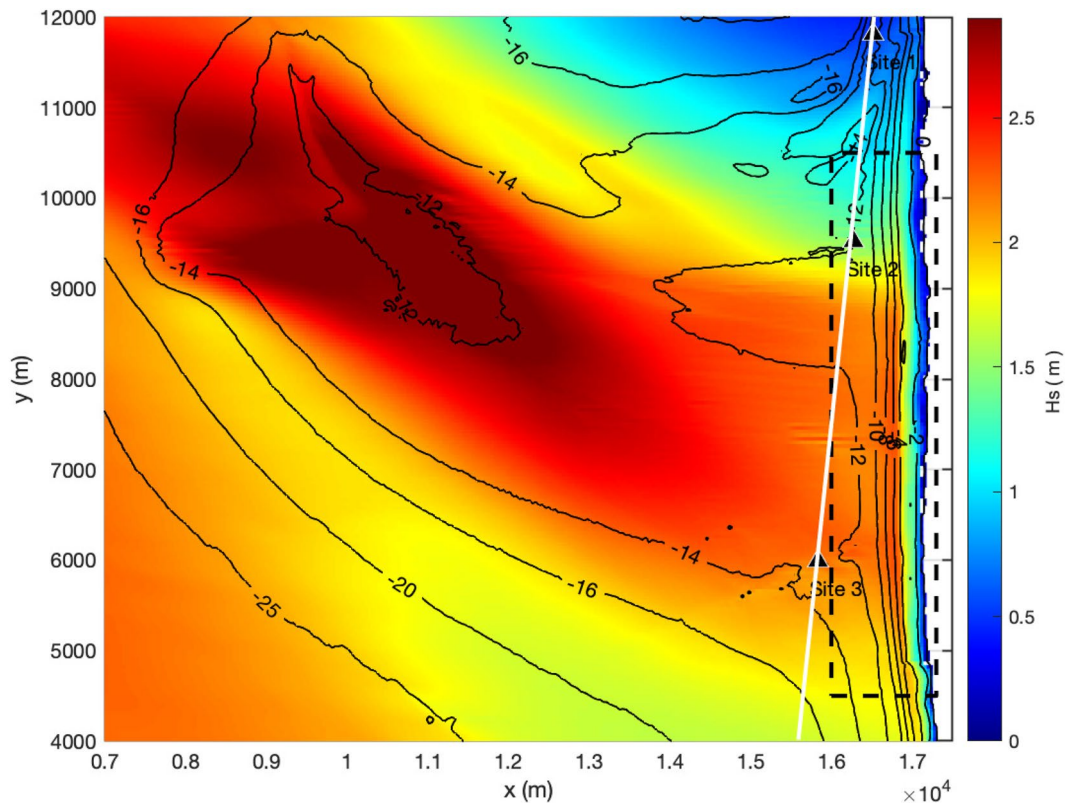


Figure 10. Wave height distribution from the Simulating WAves Nearshore model. Case 1: $H_s = 2.49$ m, $T_p = 11.1$ s, and $\theta_p = 290^\circ$ measured at the Coastal Data Information Program 029 buoy. The rectangle bounded by black dashed lines is the region shown in Figure 13. The white line is the transect crossing the measurement locations, Site 1–Site 3.

6.2. Comparison to the Wave-Averaged Circulation Model, NearCoM

The difference in the nearshore circulation induced by the wave fields with and without the wave interference effect can be examined by the comparison between FUNWAVE and NearCoM with the same offshore wave condition. Figure 13 shows the same plot as Figure 11 but from the NearCoM model for the wave condition in Case 1. As mentioned in the last section, SWAN produced the wave focusing pattern (a), the same as in FUNWAVE, though it cannot predict the small-scale fingering feature in the wave field. Responding to the wave focusing pattern, the wave setup exhibits apparently nonuniform distribution in the alongshore direction (b) with the higher setup around the wave focusing center ($y \sim 7,000$ m). The southward alongshore currents are generated by the obliquely incident waves in the south region ($y < 8,500$ m). The northward reversal flows appear in the north region ($y > 8,500$ m) as a result of the pressure gradient forcing opposite to the wave forcing direction.

For the storm scenario in Case 2, NearCoM predicted the offshore circulation on the shoal and nearshore circulation as shown in Figure 14, similar to the results from FUNWAVE. In comparison to the FUNWAVE results (Figure 12), the wave-induced offshore currents produced by NearCoM are distributed more evenly on the shoal without the small-scale strip features as shown in Figure 12. The vertical vorticity in FUNWAVE is more intense nearshore, probably due to the averaging in a short time period.

In general, the NearCoM model predicted wave-averaged processes which are similar to those predicted by FUNWAVE. However, the wave-induced circulation field predicted by NearCoM does not show much alongshore variation or small-scale structures. In addition, the wave-induced currents in NearCoM are less energetic than FUNWAVE, which will be discussed in the next section.

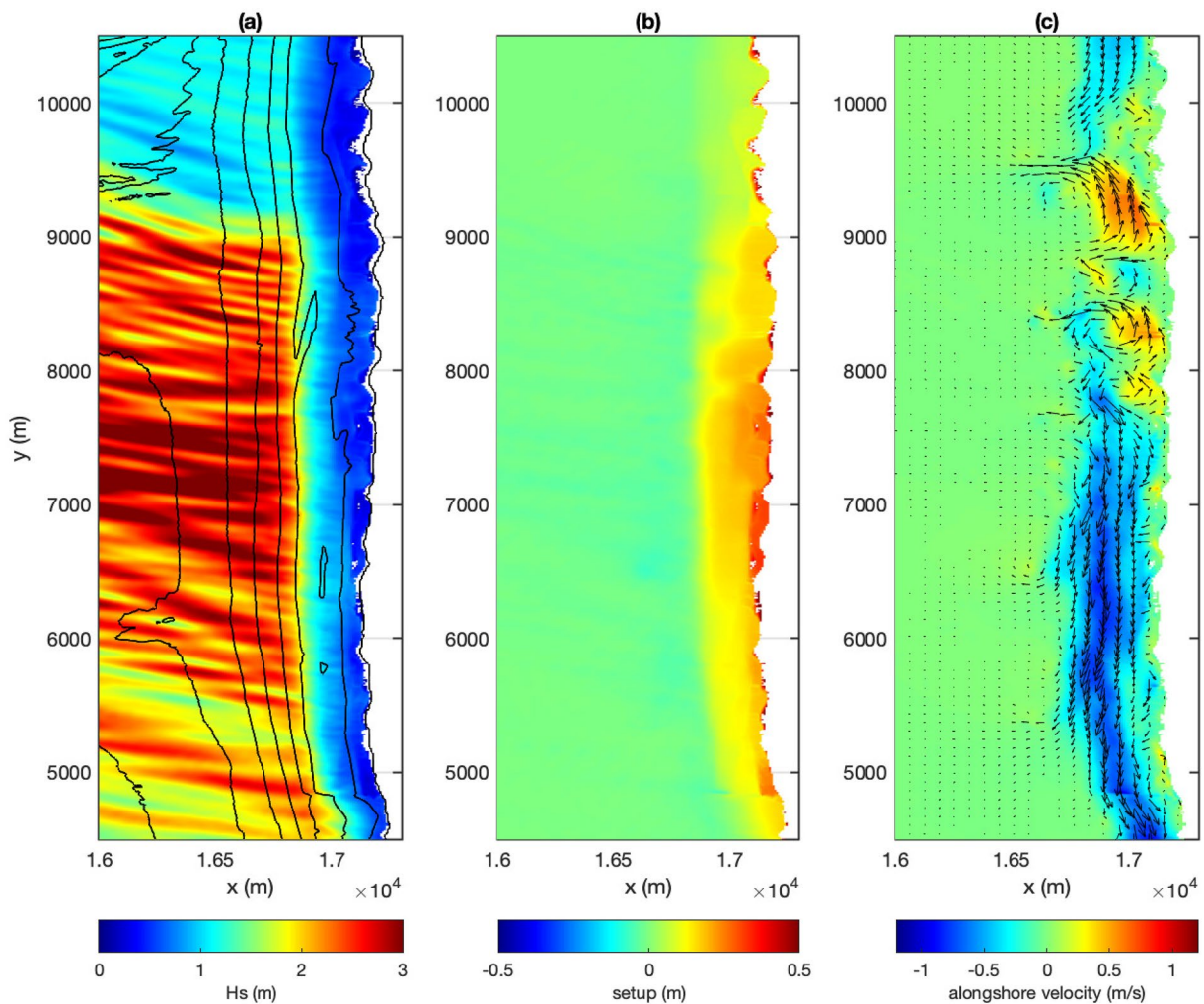


Figure 11. Wave height distribution (a), wave setup (b), and wave-induced circulation (c, color represents alongshore velocity) in the nearshore region denoted in the dashed line block in Figure 8. The wave-averaged quantities are analyzed over the time period of 1200 s. Case 1: $H_s = 2.49$ m, $T_p = 11.1$ s, and $\theta_p = 290^\circ$ measured at the Coastal Data Information Program 029 buoy.

6.3. Temporal Variability of Wave-Induced Processes

Surf zone dynamics associated with wave breaking and wave-induced processes involve a wide range of temporal scales (Geiman et al., 2011). The time-domain Boussinesq model can provide a temporal variability of wave-driven nearshore circulation under the random wave forcing and wave-current interaction (Chen et al., 2003). The energetics of wave-driven current and the associated vertical vorticity field can be obtained by time-averaging of the instantaneous wave velocity field over a relatively short time period, such as 20's wave peak periods as suggested by Chen et al. (2003). The vertical vorticity is generated by individual random breakers in the surfzone, producing shear waves different from those driven by a wave-averaged circulation model (Chen et al., 2003). To examine the correlation between wave interference and wave-induced circulation field, we demonstrate the vortex injection in the early stage of vorticity generation before shear waves are fully developed.

Figure 15 shows the results analyzed in the time period of 1800 s–2040 s (20 peak periods). In the figure, a snapshot of surface elevation (a) is also presented to show wave interference patterns. The distribution of wave height (b) looks similar to that in Figure 11a except the modulation patterns are more striking due to the shorter time processing versus the longer time processing (1200 s). As mentioned earlier, the nodal lines caused by wave interference are persistent and would not change much with time. Panel (c) shows the early stage of vertical vorticity generation, revealing that the injection of vortex eddies closely coincides with the fingering patterns of the offshore wave field.

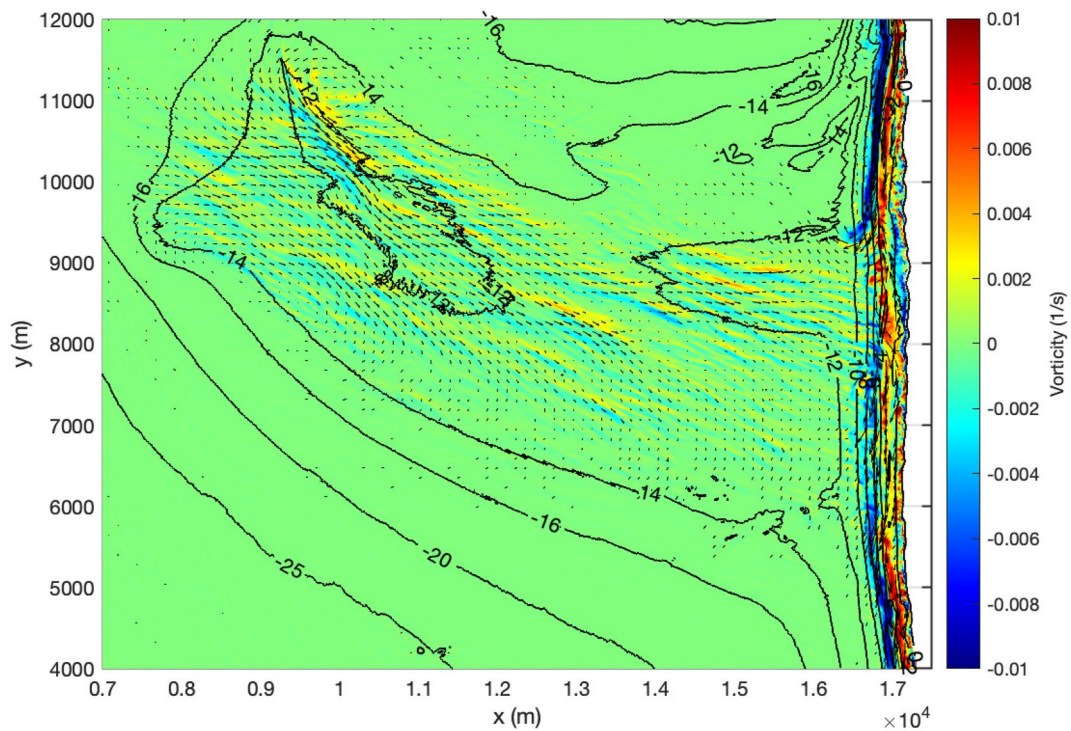


Figure 12. Current (arrows) and vorticity field (color) for Case 2. The wave-averaged quantities are analyzed in the time period of 1200 s. Wave conditions: $H_s = 5.1$ m, $T_p = 14.29$ s, and $\theta_p = 297^\circ$ measured at the Coastal Data Information Program 029 buoy.

To confirm the correlation between the wave modulation and vorticity generation, we applied Fast Fourier Transform (FFT) to both the alongshore fluctuation of wave height and vertical vorticity along the transects denoted by the white dashed lines in Figures 15b and 15c. Figure 16 compares the amplitudes of FFT for wave height and vorticity modulations versus alongshore scales. The amplitudes in the comparison were normalized by their maximum values of FFT. For the spatial modulation of wave height (blue), the peak of the FFT amplitude appears at 220 m, meaning that the alongshore scale of the nodal lines is around 220 m. As expected, the peak for the vorticity field (red) occurs around the same place, indicating the major length scale for vortices in the early stage is consistent with the scale of the nodal lines. The vorticity generation is closely correlated to the wave interference caused wave height modulation.

The energetic and transport features of vertical vorticity can be found in the snapshots of the vorticity field in Figure 17, which are taken 600 s apart, starting from $t = 2040$ s. The vertical vorticity in each snapshot was calculated by averaging over the same short time period (240 s) as the case above. The figure shows that the instantaneous vorticity is advected by alongshore currents (refer to Figure 11) southward in the south region ($y < 8,000$ m) and northward in the north region. Small-scale rip current cells appear all over the place inside the surf zone.

6.4. Explanation for the Absence of Small-Scale Modulation in Wave Setup

The wave interference-induced small-scale fingering structures in the wave height distribution do not result in significant alongshore variation in wave setup, which was unexpected based on the implications of previous studies of breaking wave-induced wave setup and nearshore circulation (e.g., Bowen, 1969, and many others). This result is studied here by examining wave-averaged cross-shore and alongshore momentum balances for the idealized case of short-crested waves formed by two intersecting plane waves propagate onto a plane beach. The beach slope is 0.0143, which is close to the beach slope in Ocean Beach. The waves are generated at a depth of 8 m using two wave components with the equal wave heights of 1.5 m, periods of 12 s, and incident wave angles of $\pm 20^\circ$ relative to shore-normal. In the following we take x to be directed onshore and y directed alongshore,

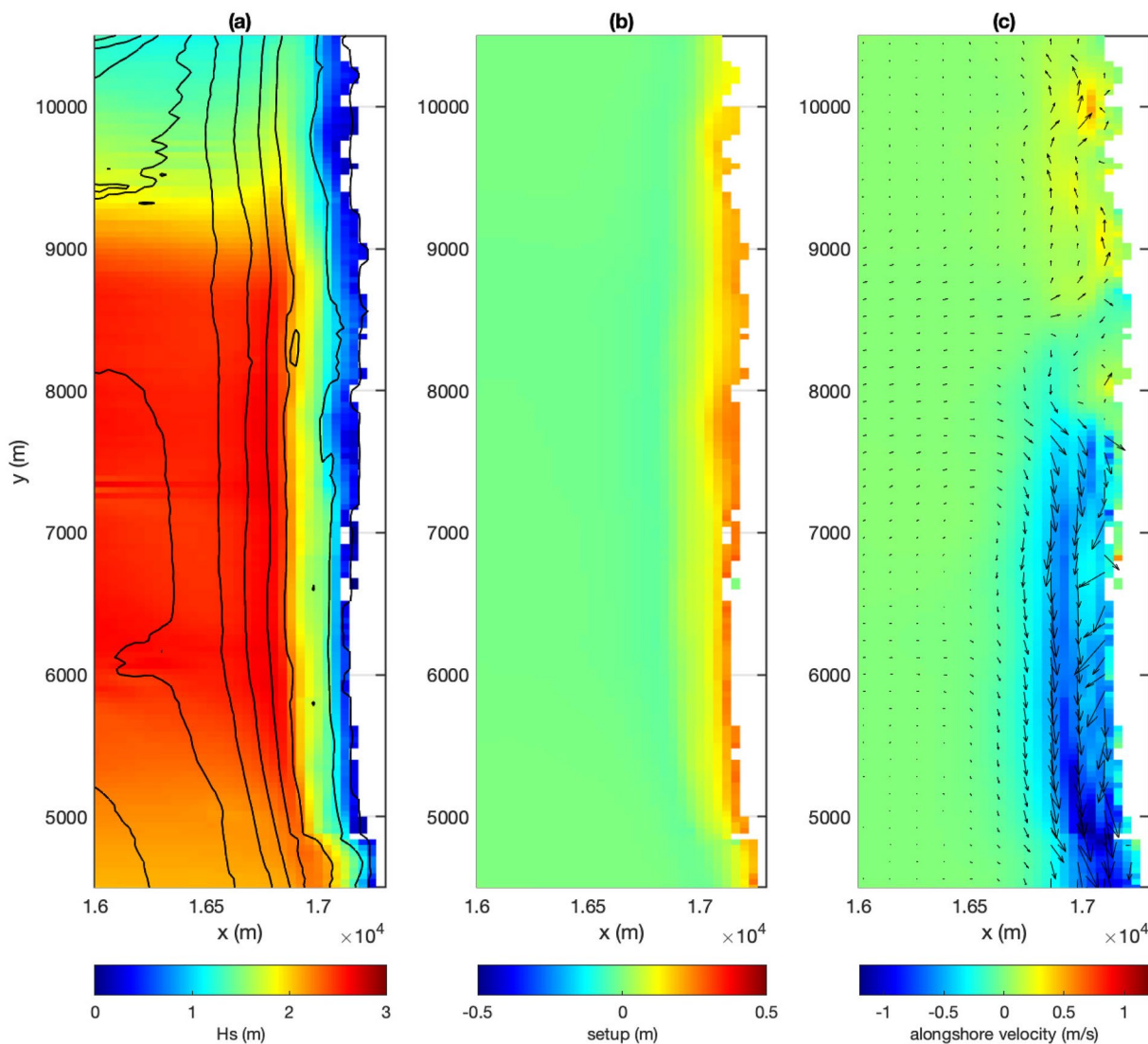


Figure 13. Simulating WAves Nearshore model result. Wave height distribution (a), wave setup (b), and wave-induced circulation (c, color represents alongshore velocity) in the nearshore region denoted in the dashed line block in Figure 10. Wave condition: $H_s = 2.49$ m, $T_p = 11.1$ s, and $\theta_p = 290^\circ$ measured at the Coastal Data Information Program 029 buoy.

with the origin at the still-water shoreline and chosen to coincide in the alongshore direction with an antinode of the short crested wave pattern.

Figure 18 shows a snapshot of (a) instantaneous surface elevation, (b) wave height distribution, (c) wave setup, and (d) wave-induced circulation. Wave averaged properties, including wave height, wave setup, and current velocity, were obtained by time-averaging over 20 wave periods after a spin-up time period of 360 s. Contributions to the x and y momentum balances were calculated for two cross-shore profiles denoted by solid white lines and labeled X1 and X2 in Figure 18a, with X1 corresponding to an antinodal position and X2 corresponding (initially) to a nodal position. We note that distortion of the wave field by the evolving rips seen in the nodes makes interpretation of contributions along X2 difficult. Contributions to the momentum balances are also computed for y -direction transects Y1–Y4, with Y1 located offshore at $x = -672$ m, close to the model wave-maker, Y2 at $x = -332$ m, just landward of the initial breaking, Y3 at $x = -122$ m, close to where the alongshore distribution of wave height becomes relatively uniform, and Y4 at $x = -22$ m, close to the shoreline.

We first discuss the main characteristics of the results shown in Figure 18. The plot of free surface elevation in Figure 18a shows the evolution of the wave from its initial configuration to a characteristic hexagonal pattern as

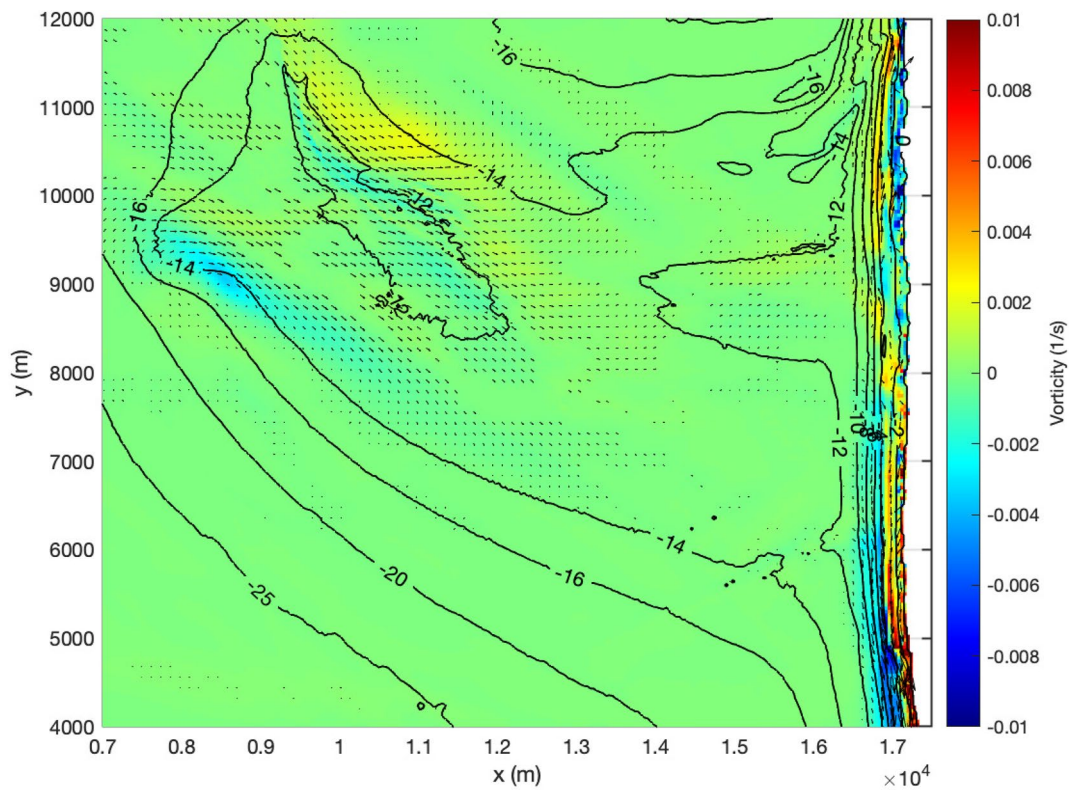


Figure 14. The same plot as Figure 12 but from the NearCoM model. Case 2: $H_s = 5.1$ m, $T_p = 14.29$ s, and $\theta_p = 297^\circ$ measured at the Coastal Data Information Program 029 buoy.

the wave shoals (Hammack et al., 1989), with more or less uniform crest heights along segments connected by saddle regions of much lower wave height. It is thus expected that the initiation of breaking would occur more or less uniformly along the elongated crest segments, leaving initially unbroken waves in the relatively narrow saddle (or nodal) regions (Figure 18b). In response, relatively concentrated rips form and flow offshore in the nodal regions (Hammack et al., 1991). Figure 18d shows the resulting wave-averaged circulation and the pattern of mean current vorticity.

The pattern of forcing resulting from wave breaking is first interpreted in the context of the depth-integrated vortex-force formulation (Smith, 2006), which highlights the dominant influence of wave energy dissipation in the mean flow forcing. In particular, Peregrine (1998) showed that variations of dissipation rates along a breaking wave crest provide a strong localized source of vertical vorticity in the wave-resolved setting. This result has further been generalized to the wave-averaged setting by Bühler and Jacobson (2001) and Bonneton et al. (2010), the result being that generation of wave-averaged mean flow vorticity is related to the rate of change of dissipation rate in the direction normal to the principle wave direction.

The pattern of wave breaking seen in the present case thus leads to a narrow region of di-polar forcing in the nodal region, thus driving the offshore-directed rip in each node. Figure 18d suggested that this effect is strongest near the Y2 transect, more or less coinciding with the initiation of breaking. It is also implied that the forcing drops to zero around the Y3 transect, where wave height has become nearly uniform alongshore. The rip current behavior is forced locally near the breaker line, rather than by possible gradients in (e.g.,) setup closer to shore. Figure 18c shows that the pattern of setup is basically uniform in the alongshore direction both near the shoreline and in the outer surfzone, with variations offshore likely suppressed by the lateral flow of water toward the nodal line to feed the dissipation-driven rip.

The x and y -direction momentum balances are next examined using the concept of radiation stresses introduced by Longuet-Higgins and Stewart (1964). The major terms in the momentum balances can be presented by the wave-averaged, depth-integrated shallow water equations for time-steady flow,

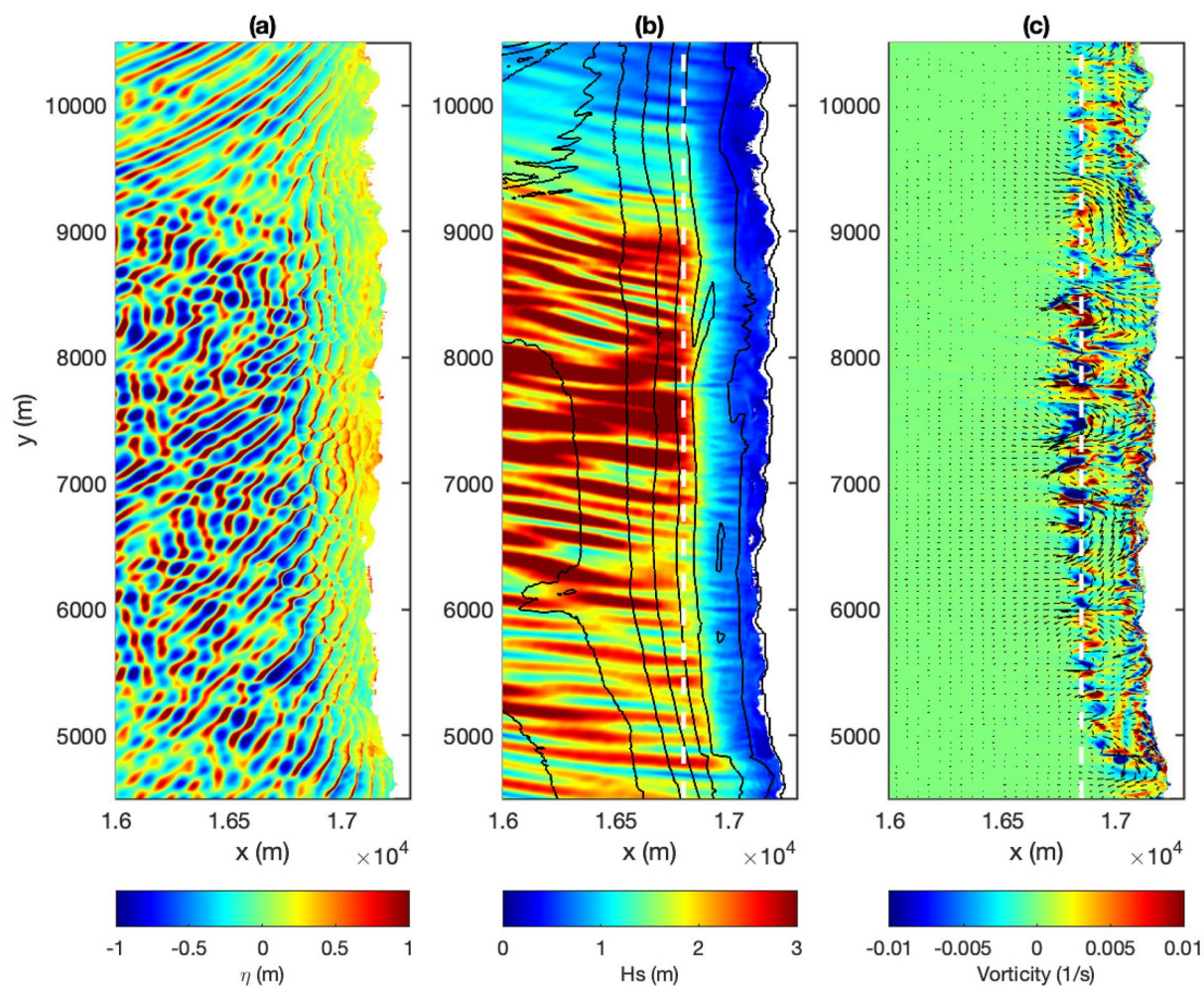


Figure 15. A snapshot of surface elevation (a), distributions of wave height (b) and vertical vorticity (c) in the nearshore region denoted in the dashed line block in Figure 8. The wave-averaged quantities are processed in the time period of 1800–2040 s (20 peak periods). Case 1: $H_s = 2.49$ m, $T_p = 11.1$ s, and $\theta_p = 290^\circ$ measured at the Coastal Data Information Program 029 buoy. White dashed lines are transects used for the Fast Fourier Transform processing.

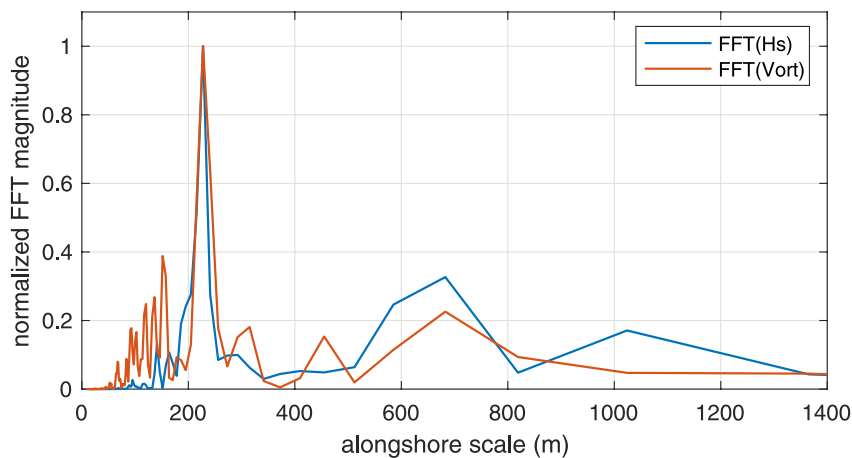


Figure 16. Amplitudes of the Fast Fourier Transform (FFT) for alongshore wave modulation (blue) and vorticity modulation (red) along the transects denoted by the white dashed lines in Figures 15b and 15c. The amplitudes were normalized by the corresponding maximum FFT values.

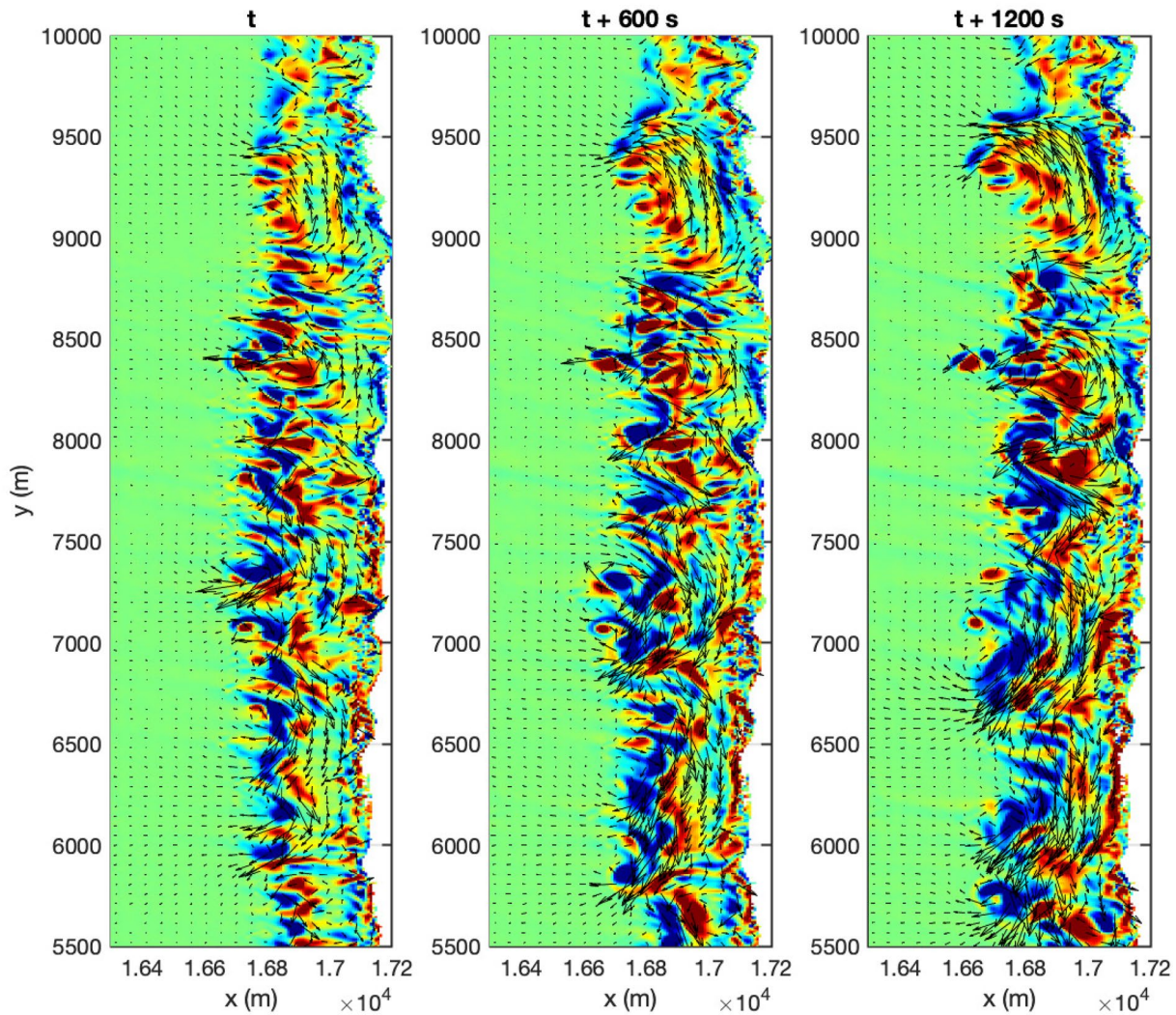


Figure 17. Time sequence of current and vorticity field averaged over 240 s. Case 1: $H_s = 2.49$ m, $T_p = 11.1$ s, and $\theta_p = 290^\circ$ measured at the Coastal Data Information Program 029 buoy.

$$\frac{\partial \bar{P}\bar{P}/H}{\partial x} + \frac{\partial \bar{P}\bar{Q}/H}{\partial y} + gH \frac{\partial \bar{\eta}}{\partial x} + \frac{\partial S_{xx}}{\partial x} + \frac{\partial S_{xy}}{\partial y} + gH \frac{\partial \bar{\eta}}{\partial x} + \bar{\tau}_x + R_x = 0, \quad (1)$$

$$\frac{\partial \bar{Q}\bar{Q}/H}{\partial y} + \frac{\partial \bar{P}\bar{Q}/H}{\partial x} + gH \frac{\partial \bar{\eta}}{\partial y} + \frac{\partial S_{yy}}{\partial y} + \frac{\partial S_{xy}}{\partial x} + gH \frac{\partial \bar{\eta}}{\partial y} + \bar{\tau}_y + R_y = 0, \quad (2)$$

where $\bar{(\cdot)}$ represents wave-averaging. $H = h + \bar{\eta}$, is the wave-averaged water depth with h and η representing the still water depth and surface elevation, respectively. In the Cartesian coordinates (x, y) , (\bar{P}, \bar{Q}) are wave-averaged volume fluxes in (x, y) directions. $(\bar{\tau}_x, \bar{\tau}_y)$ represent the bottom friction. g is the gravitational acceleration constant. The calculation of radiation stresses S_{xx} , S_{yy} , and S_{xy} can be found in Appendix A. In Equations 1 and 2, R_x and R_y are residual momentum terms in the momentum balances in x – and y – directions, respectively. da Silva et al. (2021) proposed an efficient method to calculate depth-integrated, phase-averaged momentum balances in a non-hydrostatic, phase-resolving model. They pointed out that internally calculating the depth-integrated mean momentum terms within the phase-resolving model is more accurate than the traditional post-processing method. Here, we also used the internal calculation method. Because our focus is to investigate the main momentum

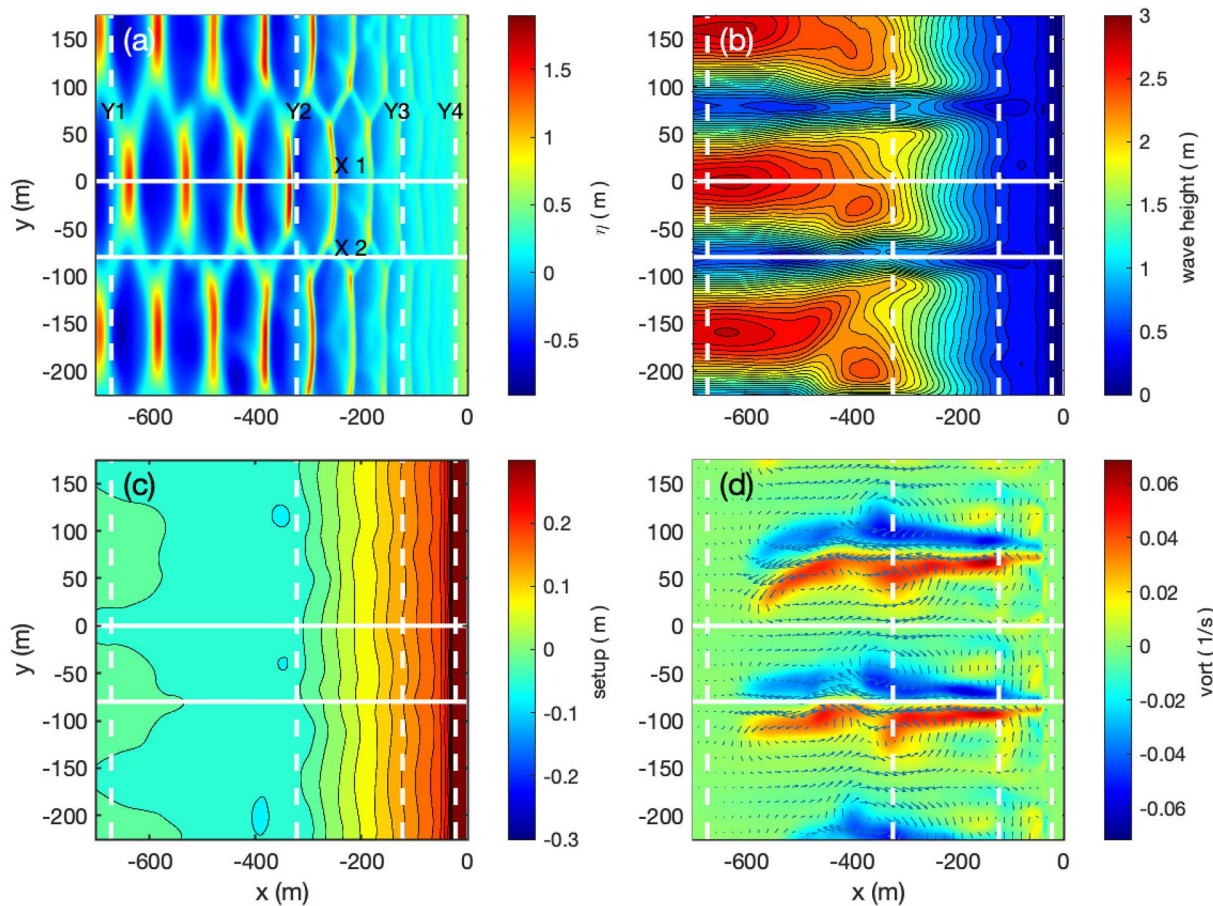


Figure 18. An idealized case of short-crested waves formed by two intersecting plane waves. (a) A snapshot of wave surface elevation; (b) wave height; (c) wave setup; (d) current field (vectors) and vertical vorticity (color). White solid lines represent two cross-shore sections along the anti-nodal line (X1) and the nodal line (X2), and white dashed lines indicate four alongshore sections (Y1–Y4), used to display results in Figures 19 and 20.

balances in the quasi-steady system, we collected the depth-integrated, phase-averaged local acceleration terms, dispersive terms, and diffusive terms in lumped residual momentum terms.

Figure 19 shows the individual contributions to the momentum balances in x – and y – directions along the antinodal profile X1 (a, c), and nodal profile X2 (b, d) lines, respectively. For the momentum balance in the x – direction, the cross-shore pressure gradients $gH\frac{\partial\bar{\eta}}{\partial x}$ along anti-nodal line (a) and nodal line (b) appear to be large and comparable to each other, indicating the significant wave setup nearshore, but minor difference in wave setup between the antinodal and nodal lines. Along the antinodal line, the cross-shore pressure gradient is basically balanced by the gradient of radiation stress $\frac{\partial S_{xx}}{\partial x}$. The advective terms $\frac{\partial \bar{P}P/H}{\partial x}$ and $\frac{\partial \bar{P}\bar{Q}/H}{\partial y}$ have different signs, and nearly cancel each other. The bottom friction is small along the entire profile. Large values of residual momentum term R_x appear in several locations, which may indicate large local accelerations.

Along the nodal line (Figure 19b), radiation stresses are much smaller, especially in the nearshore region ($x > -250$ m), due to smaller waves compared to that along the antinodal line. The pressure gradient is mainly balanced by the combination of the two advection terms, in which the magnitude of $\frac{\partial \bar{P}P/H}{\partial x}$ is larger than that of $\frac{\partial \bar{P}\bar{Q}/H}{\partial y}$ due to the rip current jet. Again, the bottom friction is insignificant, but the magnitude of which is relatively larger than that along the antinodal line because of the strong seaward flow. The magnitude of the residual momentum term R_x is large in the offshore region because of the unstable currents.

For the momentum balance in the y -direction, the pressure gradient $gH\frac{\partial\bar{\eta}}{\partial y}$ along the antinodal line (Figure 19c) is small, and all momentum terms appear to be subtle in magnitude, especially in the nearshore region. Along

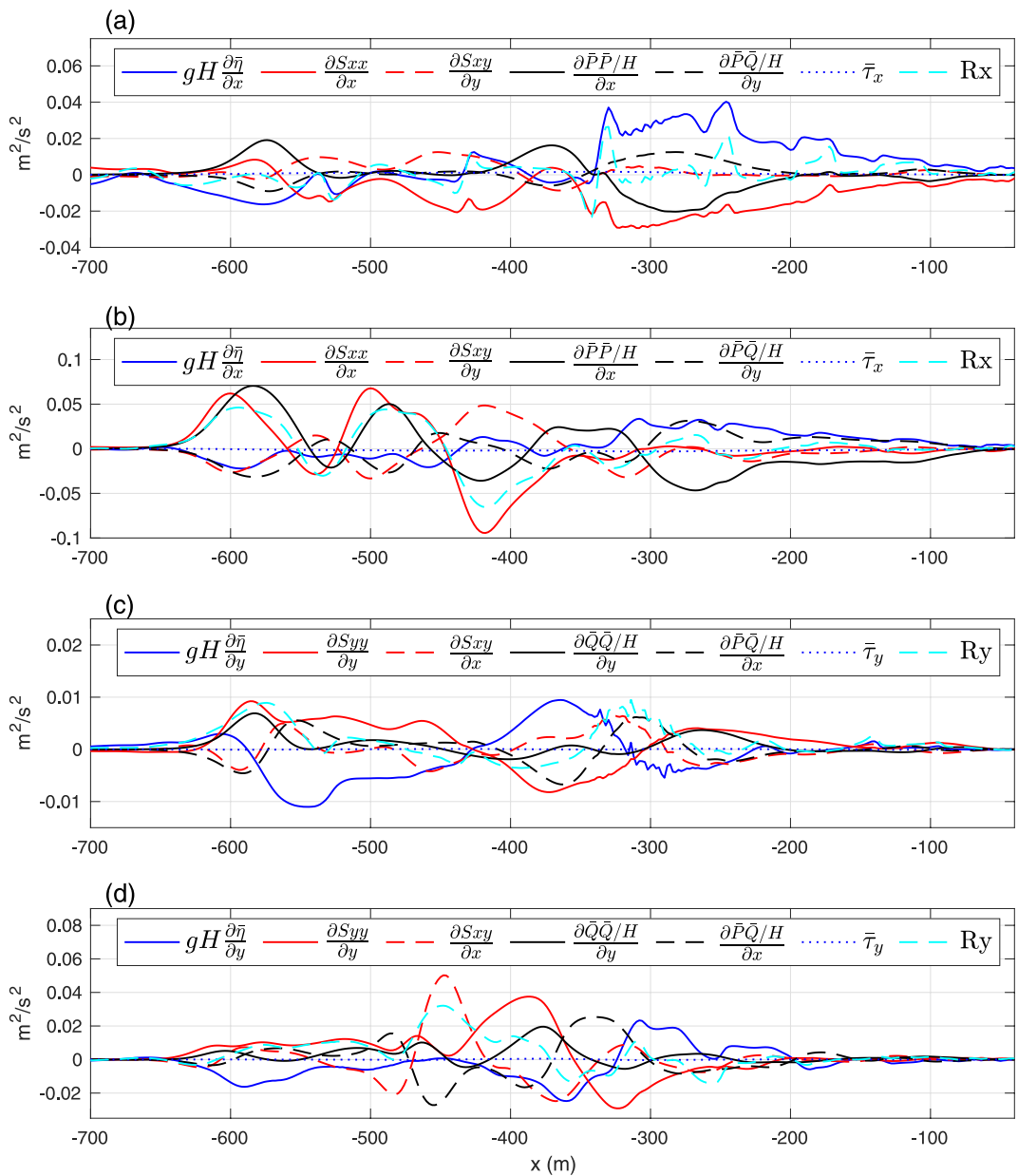


Figure 19. Contributions to x and y -direction momentum balances along the cross-shore anti-nodal section, X1, and nodal section, X2, indicated in Figure 18. x -direction components on (a) X1, (b) X2, y direction components on (c) X1, (d) X2.

the nodal line (Figure 19d), the alongshore pressure gradient is mainly balanced by the advection term $\frac{\partial \bar{P}\bar{Q}/H}{\partial x}$ in the nearshore region ($x > -250$ m). However, in the offshore region, the magnitude of the alongshore pressure gradient increases seaward. It is balanced by a combination of the gradient of radiation stresses and advection. The bottom friction in the y -direction remains small along both the antinodal and nodal lines.

Figure 20 shows the contributions to the y -direction momentum balance along the four transects Y1–Y4. Along Y1 (Figure 20a), the momentum balance is between the setdown and the lateral variation of S_{yy} , as expected in the short crested wave field. This balance continues to be seen to some extent on transects Y2 (outer surfzone) and Y3 (where wave height becomes alongshore uniform), although the pattern becomes more complex due to the hexagonal configuration of the evolving waves. The x derivatives of S_{xy} and momentum flux PQ/H become pronounced on transect Y2, where changes in wave properties in the cross-shore direction become more pronounced. Contributions to the y momentum balance then decay rapidly across the surfzone.

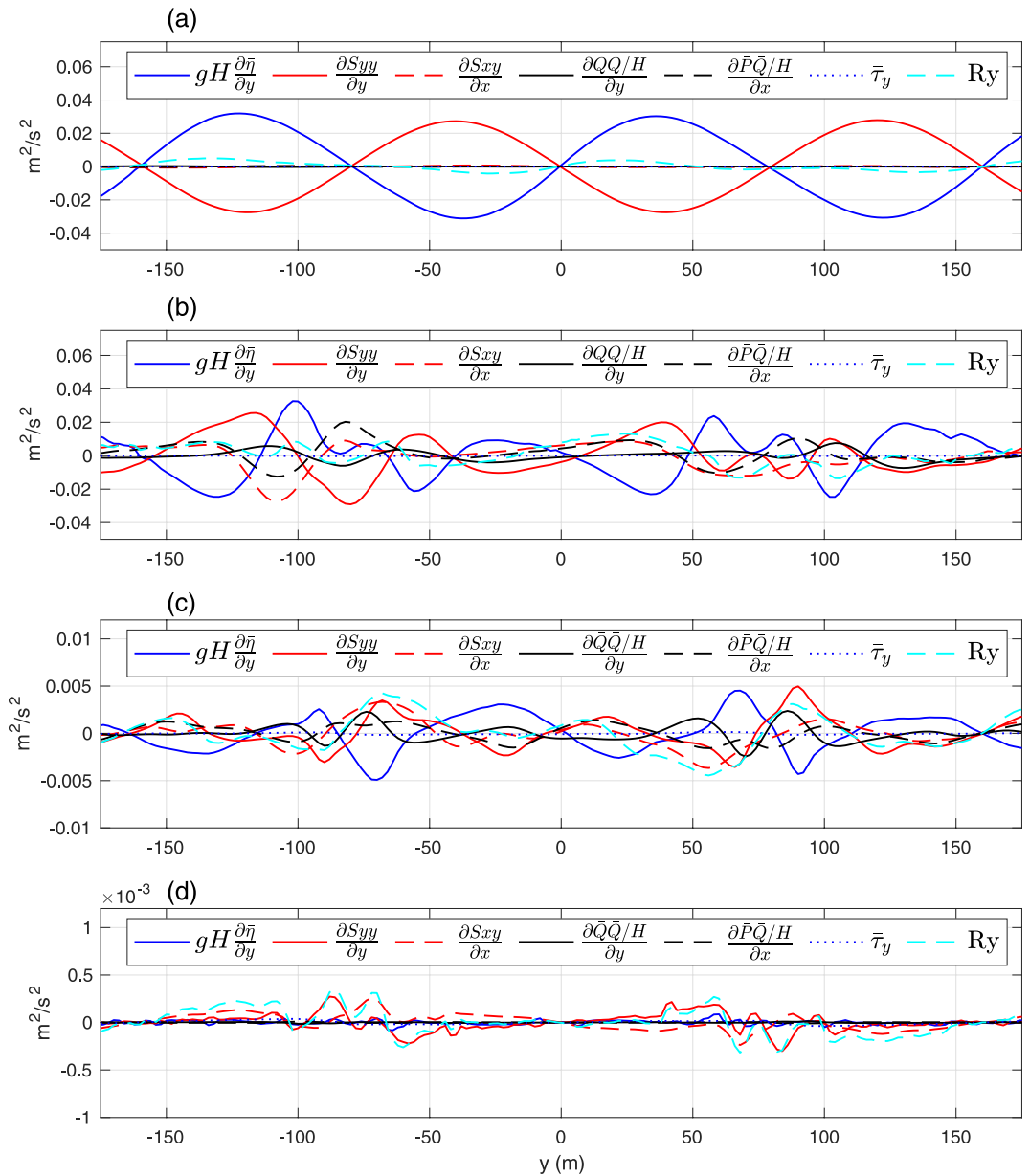


Figure 20. Contributions to the y -direction momentum balance on the alongshore sections, Y1(a), Y2 (b), Y3 (c) and Y4 (d) denoted by white dashed lines in Figure 18.

Overall, Figures 19 and 20 show that there is very little activity in the mean flow landward of $x = -200$ (m), just offshore of transect Y3, aside from the increasing setup slope which is balanced by radiation stress gradient in antinodal regions (as conventionally expected) and by cross-shore advection in nodal regions. It is noted that the rip currents cause strong perturbations to the displayed contributions offshore of the surfzone, where S_{xy} should be zero in the short-crested wave, and where x derivatives should be weak and limited to shoaling effects.

7. Conclusions

The study was motivated by the finding in Smit et al. (2016) who observed the outstanding wave interference phenomena at the ebb-tidal delta of San Francisco, CA. Our curiosity is how the wave interference affects the near-shore wave field and wave-induced nearshore circulation, which has been studied previously using wave-averaged circulation models. In this study, we used the time-domain Boussinesq wave model, FUNWAVE-TVD, to

investigate waves and wave-induced circulation processes with emphasizing wave interference caused by the ebb shoal and its effects on nearshore circulation. The model results were compared with the wave-averaged model, NearCoM, used in a previous study.

The Boussinesq model predicted the wave interference phenomena caused by the ebb shoal, with interference scales of $150 \sim 310$ m, consistent with the Radar observation by Smit et al. (2016). The model shows the small-scale fingering structures in the wave height distribution resulting from wave interference, which are persistent with nodal lines unchanged with time. The spatial variation of wave height can reach up to 50% of the wave height predicted by the conventional phase-averaged wave model. The field observation offshore of Ocean Beach in the previous studies did not resolve the wave field modulation due to the sparse deployments of instruments.

The impact of wave interference on nearshore circulation is significant. The modulated wave field induces small-scale flow structures in nearshore circulation, which were not predicted by the conventional wave-averaged circulation model. However, the small-scale modulation in the wave field seems not to generate alongshore variation in wave setup in such scales. Therefore, in a large-scale view, the alongshore currents predicted by the Boussinesq model still keep the major features shown in the wave-averaged circulation model, such as the flow divergence caused by the pressure gradient force associated with the wave setup. For a storm wave condition, waves break on the ebb shoal, inducing shoreward-directed currents in the breaking region, indicated in both the Boussinesq and the wave-averaged circulation model. The Boussinesq model shows smaller-scale stripe features of breaking wave-induced current and vorticity fields versus the wave-averaged circulation model in which the current and vorticity are evenly distributed on the shoal. It is not clear that the stripe-like vorticity distribution is directly related to the coherent wave interference.

The time-domain Boussinesq model predicted the temporal variability of wave-induced processes. The wave field modulation is highly correlated to the vorticity generation nearshore. The alongshore varying wave breakers tied with wave interference patterns are sources of the vorticity generation and cause energetic vortex eddies in the surf zone.

To explain why the wave interference-induced small-scale alongshore variation of wave height do not result in alongshore variation of wave setup at the similar scales, we carried out an idealized simulation of short crest waves formed by two intersecting plane waves propagating on a plane beach. The momentum balances at the time-averaged scale show that, in the antinodal region, the cross-shore pressure gradient is mainly balanced by the gradient of radiation stresses, while in the nodal region, it is mainly balanced by the flow advection. The rip current behavior is forced locally near breakers, rather than by gradients in wave setup close to shore.

The nearshore circulation at Ocean Beach is affected by tides and tidal currents, especially in the nearshore area close to the inlet as discussed in Shi et al. (2011) and Hansen et al. (2013). Due to a large computational cost, we did not include tides in the time-domain Boussinesq model. However, the model reveals more complete physical processes associated with wave interference effects and provides a promising prospect for the future research on wave-induced processes in the large ebb shoal-beach system.

Appendix A: Formulations of Radiation Stresses

The radiation stresses can be expressed by

$$S_{xx} = \overline{\int_{-h}^{\eta} (u^2 - w^2) dz} + \frac{1}{2} g \overline{\eta^2}, \quad (A1)$$

$$S_{yy} = \overline{\int_{-h}^{\eta} (v^2 - w^2) dz} + \frac{1}{2} g \overline{\eta^2}, \quad (A2)$$

$$S_{xy} = \overline{\int_{-h}^{\eta} u v dz}, \quad (A3)$$

where (u, v, w) represent velocity components in (x, y, z) directions. In this study, the velocity components were estimated by modeled velocity field accurate up to $O(\mu^2)$, (where μ is a parameter characterizing the ratio of water depth to wave length, see Shi et al., 2012, for details). To make it convenient to remove wave-averaged current

velocity from the instantaneous velocity, we used the depth-averaged velocity $\bar{\mathbf{u}} = \mathbf{u}_a + \bar{\mathbf{u}}_2$, in which \mathbf{u}_a denotes the velocity at a reference elevation and $\bar{\mathbf{u}}_2$ is the depth averaged $O(\mu^2)$ contribution to the horizontal velocity field. The vertical component w was estimated by $w(x, y, z, t) = -\mu^2 \nabla \cdot [(h+z)\mathbf{u}_a]$. For the specific application in this study, the depth-averaged vertical velocity \tilde{w} was roughly estimated as half of the vertical velocity at the surface, that is, $\tilde{w} = w(x, y, \eta, t)/2$. The final expressions of radiation stresses are

$$S_{xx} = \overline{[(\tilde{u} - \tilde{u}_m)^2 - \tilde{w}^2]}(h + \eta) + \frac{1}{2}g\overline{\eta^2}, \quad (A4)$$

$$S_{yy} = \overline{[(\tilde{v} - \tilde{v}_m)^2 - \tilde{w}^2]}(h + \eta) + \frac{1}{2}g\overline{\eta^2}, \quad (A5)$$

and

$$S_{xy} = \overline{(\tilde{u} - \tilde{u}_m)(\tilde{v} - \tilde{v}_m)(h + \eta)}, \quad (A6)$$

where $(\tilde{u}_m, \tilde{v}_m)$ represent the wave-averaged, depth-averaged velocities in (x, y) directions. It should be mentioned that the ordering of the terms in the radiation stresses above is not exactly consistent with the derivation of the fully nonlinear Boussinesq model (Wei et al., 1995). Errors may exist in $O(\mu^4)$ contributions.

Calculations of time averaged quantities $(\tilde{u}_m, \tilde{v}_m)$, (\bar{P}, \bar{Q}) and the radiation stresses, S_{xx} , S_{xy} , S_{yy} , were integrated in specified time segments, such as 20 wave periods. In the calculations of the instantaneous wave velocity, such as $\tilde{u} - \tilde{u}_m$, the averaged value \tilde{u}_m is from the averaging in the last time segment.

Data Availability Statement

The post-processed numerical results and measurement data used in this research are archived at (<http://doi.org/10.5281/zenodo.6336156>).

Acknowledgments

The authors wish to thank Pieter Smit and two anonymous reviewers for their constructive comments and suggestions. The first author, Yu Zhang, would like to thank the Center for Applied Coastal Research at the University of Delaware for hosting her study visit. James T. Kirby and Fengyan Shi were partially supported by the Office of Naval Research, award no. N00014-21-1-2786. The corresponding author, Fengyan Shi, would like to express his appreciation for the support of the College of Engineering, University of Delaware, during his sabbatical leave. This research was supported in part through the use of Information Technologies (IT) resources at the University of Delaware. The package of FUNWAVE-TVD, including source codes, benchmark tests, and examples for various model applications is maintained at the GITHUB site: <https://github.com/fengyanshi/FUNWAVE-TVD>.

References

- Akrish, G., Smit, P., Zijlema, M., & Reniers, A. (2020). Modelling statistical wave interferences over shear currents. *Journal of Fluid Mechanics*, 891, A2. <https://doi.org/10.1017/jfm.2020.143>
- Barnard, P. L., Eshleman, J., Erikson, L., & Hanes, D. M. (2007). *Coastal processes study at Ocean Beach, San Francisco, CA: Summary of data collection 2004–2006* (US Geological Survey Open-File Report No. 2007-1217). U.S. Geological Survey, U.S. Department of the Interior.
- Barnard, P. L., Hansen, J. E., & Erikson, L. H. (2012). Synthesis study of an erosion hot spot, ocean beach, California. *Journal of Coastal Research*, 28(4), 903–922. <https://doi.org/10.2112/JCOASTRES-D-11-00212.1>
- Bonneton, P., Bruneau, N., Castelle, B., & Marche, F. (2010). Large-scale vorticity generation due to dissipating waves in the surf zone. *Discrete and Continuous Dynamical Systems - Series B*, 13(4), 729–738. <https://doi.org/10.3934/dcdsb.2010.13.729>
- Booij, N., Ris, R. C., & Holthuijsen, L. H. (1999). A third-generation wave model for coastal regions: 1. Model description and validation. *Journal of Geophysical Research*, 104(C4), 7649–7666. <https://doi.org/10.1029/98JC02622>
- Bouws, E., Günther, H., Rosenthal, W., & Vincent, C. (1985). Similarity of the wind wave spectrum in finite depth water: 1. Spectral form. *Journal of Geophysical Research*, 90(C1), 975–986. <https://doi.org/10.1029/jc090ic01p00975>
- Bowen, A. J. (1969). Rip currents: 1. Theoretical investigations. *Journal of Geophysical Research*, 74(23), 5467–5478. <https://doi.org/10.1029/jc074i023p05467>
- Brown, J., MacMahan, J., Reniers, A., & Thornton, E. (2009). Surf zone diffusivity on a rip-channelled beach. *Journal of Geophysical Research*, 114(C11), C11015. <https://doi.org/10.1029/2008jc005158>
- Bühler, O., & Jacobson, T. E. (2001). Wave-driven currents and vortex dynamics on barred beaches. *Journal of Fluid Mechanics*, 449, 313–339. <https://doi.org/10.1017/S0022112001006322>
- Chakrabarti, A., Brandt, S. R., Chen, Q., & Shi, F. (2017). Boussinesq modeling of wave-induced hydrodynamics in coastal wetlands. *Journal of Geophysical Research: Oceans*, 122(5), 3861–3883. <https://doi.org/10.1002/2016jc012093>
- Chawla, A., Özkan Haller, H. T., & Kirby, J. T. (1998). Spectral model for wave transformation and breaking over irregular bathymetry. *Journal of Waterway, Port, Coastal, and Ocean Engineering*, 124(4), 189–198. [https://doi.org/10.1061/\(ASCE\)0733-950X\(1998\)124:4\(189\)](https://doi.org/10.1061/(ASCE)0733-950X(1998)124:4(189))
- Chen, J.-L., Shi, F., Hsu, T.-J., & Kirby, J. T. (2014). NearCom-TVD—A quasi-3D nearshore circulation and sediment transport model. *Coastal Engineering*, 91, 200–212. <https://doi.org/10.1016/j.coastaleng.2014.06.002>
- Chen, Q. (2006). Fully nonlinear Boussinesq-type equations for waves and currents over porous beds. *Journal of Engineering Mechanics*, 132(2), 220–230. [https://doi.org/10.1061/\(ASCE\)0733-9399\(2006\)132:2\(220\)](https://doi.org/10.1061/(ASCE)0733-9399(2006)132:2(220))
- Chen, Q., Dalrymple, R. A., Kirby, J. T., Kennedy, A. B., & Haller, M. C. (1999). Boussinesq modeling of a rip current system. *Journal of Geophysical Research*, 104(C9), 20617–20637. <https://doi.org/10.1029/1999JC900154>
- Chen, Q., Kirby, J. T., Dalrymple, R. A., Kennedy, A. B., & Chawla, A. (2000). Boussinesq modeling of wave transformation, breaking and runup. II: 2D. *Journal of Waterway, Port, Coastal, and Ocean Engineering*, 126(1), 48–56. [https://doi.org/10.1061/\(ASCE\)0733-950X\(2000\)126:1\(48\)](https://doi.org/10.1061/(ASCE)0733-950X(2000)126:1(48))
- Chen, Q., Kirby, J. T., Dalrymple, R. A., Shi, F., & Thornton, E. B. (2003). Boussinesq modeling of longshore currents. *Journal of Geophysical Research*, 108(C11), 3362. <https://doi.org/10.1029/2002JC001308>
- da Silva, R. F., Rijnsdorp, D. P., Hansen, J. E., Lowe, R., Buckley, M., & Zijlema, M. (2021). An efficient method to calculate depth-integrated, phase-averaged momentum balances in non-hydrostatic models. *Ocean Modelling*, 165, 101846. <https://doi.org/10.1016/j.ocemod.2021.101846>

- Dalrymple, R. A. (1975). A mechanism for rip current generation on an open coast. *Journal of Geophysical Research*, 80(24), 3485–3487. <https://doi.org/10.1029/JC080i024p03485>
- Dalrymple, R. A., MacMahan, J. H., Reniers, A. J., & Nelko, V. (2011). Rip currents. *Annual Review of Fluid Mechanics*, 43(1), 551–581. <https://doi.org/10.1146/annurev-fluid-122109-160733>
- Eshleman, J. L., Barnard, P. L., Erikson, L. H., & Hanes, D. M. (2007). Coupling alongshore variations in wave energy to beach morphologic change using the SWAN wave model at Ocean Beach, San Francisco, CA. In *10th international workshop on wave hindcasting and forecasting (Oahu, Hawaii)* (Vol. 4, p. 20p). Citeseer.
- Fregoso, T. A., Wang, R.-F., Ateljevich, E., & Jaffe, B. E. (2017). *A new seamless, high-resolution digital elevation model of the San Francisco Bay-Delta Estuary, California*. Tech. rep. US Geological Survey.
- Geiman, J. D., Kirby, J. T., Reniers, A. J. H. M., & MacMahan, J. H. (2011). Effects of wave averaging on estimates of fluid mixing in the surf zone. *Journal of Geophysical Research*, 116(C4), C04006. <https://doi.org/10.1029/2010JC006678>
- Hammack, J., Scheffner, N., & Segur, H. (1991). A note on the generation and narrowness of periodic rip currents. *Journal of Geophysical Research*, 96(C3), 4909–4914. <https://doi.org/10.1029/90jc02304>
- Hammack, J. L., Scheffner, N., & Segur, H. (1989). Two-dimensional periodic waves in shallow water. *Journal of Fluid Mechanics*, 209, 567–589. <https://doi.org/10.1017/S0022112089003228>
- Hansen, J. E., Elias, E., List, J. H., Erikson, L. H., & Barnard, P. L. (2013). Tidally influenced alongshore circulation at an inlet-adjacent shoreline. *Continental Shelf Research*, 56, 26–38. <https://doi.org/10.1016/j.csr.2013.01.017>
- Hansen, J. E., Janssen, T. T., Raubenheimer, B., Shi, F., Barnard, P. L., & Jones, I. S. (2014). Observations of surfzone alongshore pressure gradients onshore of an ebb-tidal delta. *Coastal Engineering*, 91, 251–260. <https://doi.org/10.1016/j.coastaleng.2014.05.010>
- Hasselmann, K., Barnett, T. P., Bouws, E., Carlson, H., Cartwright, D. E., Enke, K., et al. (1973). Measurements of wind-wave growth and swell decay during the joint north sea wave project (JONSWAP). *Ergaenzungsheft zur Deutschen Hydrographischen Zeitschrift*.
- Johnson, D. (2004). Transient rip currents and nearshore circulation on a swell-dominated beach. *Journal of Geophysical Research*, 109(C2), C02026. <https://doi.org/10.1029/2003JC001798>
- Kennedy, A. B., Chen, Q., Kirby, J. T., & Dalrymple, R. A. (2000). Boussinesq modeling of wave transformation, breaking and runup. I: 1D. *Journal of Waterway, Port, Coastal, and Ocean Engineering*, 126(1), 39–47. [https://doi.org/10.1061/\(ASCE\)0733-950x\(2000\)126:1\(39\)](https://doi.org/10.1061/(ASCE)0733-950x(2000)126:1(39))
- Kennedy, A. B., Kirby, J. T., Chen, Q., & Dalrymple, R. A. (2001). Boussinesq-type equations with improved nonlinear performance. *Wave Motion*, 33(3), 225–243. [https://doi.org/10.1016/S0165-2125\(00\)00071-8](https://doi.org/10.1016/S0165-2125(00)00071-8)
- Kirby, J. T. (2016). Boussinesq models and their application to coastal processes across a wide range of scales. *Journal of Waterway, Port, Coastal, and Ocean Engineering*, 142(6). [https://doi.org/10.1061/\(ASCE\)WW.1943-5460.0000350](https://doi.org/10.1061/(ASCE)WW.1943-5460.0000350)
- Komen, G. J., Cavalieri, L., Donelan, M., Hasselmann, K., Hasselmann, S., & Janssen, P. (1996). *Dynamics and modelling of ocean waves*. Cambridge University Press.
- Lam, M. Y., Malej, M., Shi, F., & Ghosh, K. (2018). *Profiling and optimization of FUNWAVE-TVD on high performance computing (HPC) machines*. Tech. rep. Army Engineer Waterways Experiment Station.
- Lesser, G. R., Roelvink, J. A., van Kester, J. T. M., & Stelling, G. S. (2004). Development and validation of a three-dimensional morphological model. *Coastal Engineering*, 51(8–9), 883–915. <https://doi.org/10.1016/j.coastaleng.2004.07.014>
- Longuet-Higgins, M. S., & Stewart, R. (1964). Radiation stresses in water waves; a physical discussion, with applications. In *Deep sea research and oceanographic abstracts* (Vol. 11, pp. 529–562). Elsevier.
- Ma, G., Shi, F., & Kirby, J. T. (2012). Shock-capturing non-hydrostatic model for fully dispersive surface wave processes. *Ocean Modelling*, 43(44), 22–35. <https://doi.org/10.1016/j.ocemod.2011.12.002>
- MacMahan, J., Brown, J., Brown, J., Thornton, E., Reniers, A., Stanton, T., et al. (2010). Mean Lagrangian flow behavior on an open coast rip-channelled beach: A new perspective. *Marine Geology*, 268(1–4), 1–15. <https://doi.org/10.1016/j.margeo.2009.09.011>
- Mei, C. C., Stiassnie, M., & Yue, D. K.-P. (2005). Theory and applications of ocean surface waves, part 1: Linear aspects. In *Advanced series on ocean engineering* (Vol. 23, p. 513). World Scientific.
- O'Reilly, W. C., Olfe, C. B., Thomas, J., Seymour, R., & Guza, R. (2016). The California coastal wave monitoring and prediction system. *Coastal Engineering*, 116, 118–132. <https://doi.org/10.1016/j.coastaleng.2016.06.005>
- Peregrine, D. H. (1998). Surf zone currents. *Theoretical and Computational Fluid Dynamics*, 10(1–4), 295–309. <https://doi.org/10.1007/s001620050065>
- Salatin, R., Chen, Q., Bak, A. S., Shi, F., & Brandt, S. R. (2021). Effects of wave coherence on longshore variability of nearshore wave processes. *Journal of Geophysical Research: Oceans*, 126(11), e2021JC017. <https://doi.org/10.1029/2021JC017641>
- Shi, F., Hanes, D. M., Kirby, J. T., Erikson, L., Barnard, P., & Eshleman, J. (2011). Pressure-gradient-driven nearshore circulation on a beach influenced by a large inlet-tidal shoal system. *Journal of Geophysical Research*, 116(C4), C04020. <https://doi.org/10.1029/2010JC006788>
- Shi, F., Kirby, J., Newberger, P., & Haas, K. (2005). Nearcom master program. version 2005.4: User's manual and module integration. *Research report*, 10.
- Shi, F., Kirby, J. T., & Haas, K. (2007). Quasi-3d nearshore circulation equations: A CL-vortex force formulation. In *Coastal engineering* (Vol. 5, pp. 1028–1039). World Scientific.
- Shi, F., Kirby, J. T., Harris, J. C., Geiman, J. D., & Grilli, S. T. (2012). A high-order adaptive time-stepping TVD solver for Boussinesq modeling of breaking waves and coastal inundation. *Ocean Modelling*, 43, 36–51. <https://doi.org/10.1016/j.ocemod.2011.12.004>
- Smit, P. B., Bland, R., Janssen, T. T., & Laughlin, B. (2016). Remote sensing of nearshore wave interference. *Journal of Geophysical Research: Oceans*, 121(5), 3409–3421. <https://doi.org/10.1002/2016JC011705>
- Smit, P. B., & Janssen, T. T. (2013). The evolution of inhomogeneous wave statistics through a variable medium. *Journal of Physical Oceanography*, 43(8), 1741–1758. <https://doi.org/10.1175/JPO-D-13-046.1>
- Smit, P. B., Janssen, T. T., & Herbers, T. H. C. (2015). Stochastic modeling of inhomogeneous ocean waves. *Ocean Modelling*, 96, 26–35. <https://doi.org/10.1016/j.ocemod.2015.06.009>
- Smith, J. A. (2006). Wave-current interactions in finite depth. *Journal of Physical Oceanography*, 36(7), 1403–1419. <https://doi.org/10.1175/jpo2911.1>
- Spydell, M., & Feddersen, F. (2009). Lagrangian drifter dispersion in the surf zone: Directionally spread, normally incident waves. *Journal of Physical Oceanography*, 39(4), 809–830. <https://doi.org/10.1175/2008jpo3892.1>
- Tolman, H. L. (1991). A third-generation model for wind waves on slowly varying, unsteady, and inhomogeneous depths and currents. *Journal of Physical Oceanography*, 21(6), 782–797. [https://doi.org/10.1175/1520-0485\(1991\)021<782:atgmfw>2.0.co;2](https://doi.org/10.1175/1520-0485(1991)021<782:atgmfw>2.0.co;2)
- Vincent, C. L., & Briggs, M. J. (1989). Refraction-diffraction of irregular waves over a mound. *Journal of Waterway, Port, Coastal, and Ocean Engineering*, 115(2), 269–284. [https://doi.org/10.1061/\(ASCE\)0733-950x\(1989\)115:2\(269\)](https://doi.org/10.1061/(ASCE)0733-950x(1989)115:2(269))

- Wei, G., Kirby, J. T., Grilli, S. T., & Subramanya, R. (1995). A fully nonlinear Boussinesq model for surface waves. Part 1. Highly nonlinear unsteady waves. *Journal of Fluid Mechanics*, 294, 71–92. <https://doi.org/10.1017/S0022112095002813>
- Wei, G., Kirby, J. T., & Sinha, A. (1999). Generation of waves in Boussinesq models using a source function method. *Coastal Engineering*, 36(4), 271–299. [https://doi.org/10.1016/s0378-3839\(99\)00009-5](https://doi.org/10.1016/s0378-3839(99)00009-5)
- Yuan, Y., Shi, F., Kirby, J., & Yu, F. (2020). Multiple-GPU acceleration of the Boussinesq-type wave model FUNWAVE-TVD. *Journal of Advances in Modeling Earth Systems*, 12(5), 1–19. <https://doi.org/10.1029/2019MS001957>
- Zijlema, M., Stelling, G., & Smit, P. (2011). SWASH: An operational public domain code for simulating wave fields and rapidly varied flows in coastal waters. *Coastal Engineering*, 58(10), 992–1012. <https://doi.org/10.1016/j.coastaleng.2011.05.015>